



Physics-informed neural networks for heat transfer prediction in two-phase flows

Darioush Jalili, Seohee Jang, Mohammad Jadidi, Giovanni Giustini, Amir Keshmiri,
Yasser Mahmoudi*

Department of Fluids and Environment, The University of Manchester, Manchester M13 9PL, United Kingdom



ARTICLE INFO

Keywords:
 Physics-informed neural networks
 Two-phase flows
 Bubble dynamics
 Heat transfer
 Multiphysics problem
 Inverse problems

ABSTRACT

This paper presents data-driven simulations of two-phase fluid processes with heat transfer. A Physics-Informed Neural Network (PINN) was applied to capture the behaviour of phase interfaces in two-phase flows and model the hydrodynamics and heat transfer of flow configurations representative of established numerical test cases. The developed PINN approach was trained on simulation data derived from physically based Computational Fluid Dynamics (CFD) simulations with interface capturing. The present study considers fundamental problems, including tracking the rise of a single gas bubble in a denser fluid and exploring the heat transfer in the wake of a bubble rising close to a heated wall. Tracking of a rising bubble phase interface of fluids with disparate properties was performed, revealing a maximum error of only 5.2% at the interface edge and a maximum error of 2.8% at the position of the centre of mass. Inferred (hidden variable) flows are studied in addition to a purely extrapolative inverse isothermal bubble case. When no velocity data was supplied, velocity field predictions remained accurate. Rise of an inferred isothermal bubble with unseen fluid properties was found to produce a maximum mean-squared error of 0.28 and centre of mass error of 1.25%. For the case of the rising bubble with a hot wall, the maximum error in the temperature domain using specified boundary conditions was 6.8%, while the bubble position analysis reveals a maximum positional error of 3.6%. These results demonstrate that PINN is agnostic to geometry and fluid properties when studying the combined effects of convection and buoyancy on two-phase flows for the first time. This work serves as a starting point for PINN in multiphase cases involving heat transfer over a range of geometries. Eventually, PINN will be used in such cases to provide solutions for forward, inverse, and extrapolative cases. Each of which represent a dramatic saving in computational cost compared to traditional CFD.

1. Introduction

The coexistence of multiple fluid phases is pervasive in both natural phenomena and engineering systems. It is encountered in a wide range of chemical and natural processes, such as boiling, distillation, absorption, flotation, and multiphase reactors [1–2]. Multiphase flows in such processes involve continuous contact of two or more phases, which is commonly achieved by a gaseous phase bubbling into a liquid phase. Though frequently observed, rising bubbles are the result of a complex and intertwined system [3], and an in-depth understanding of the bubbles is crucial to design such processes, as they influence the hydrodynamic behaviour of the chemical processes. The complex physics involved in rising bubbles include the co-dependant effects of thermal and hydrodynamic boundary layers, which influence the behaviour of

the surrounding fluid and the bubble interface. Flow separation occurs when the fluid flow around the bubble detaches from its surface, leading to the formation of vortical wakes [4]. Buoyancy plays a significant role in the upward movement of bubbles, as the density difference between the bubble and the surrounding fluid causes it to rise [5]. Moreover, the interfaces between the bubble and the surrounding fluid are not rigid but can deform due to various forces and flows, adding further complexity to the system [6]. Accurately modelling and simulating all these interconnected physical phenomena pose substantial challenges. Traditional numerical methods may struggle to capture the intricate details and interactions involved in the rising bubble phenomenon [7]. However, one promising avenue that has not yet been explored extensively in this context is the use of Physics-Informed Neural Networks (PINNs) [8].

Data-driven PINNs combine the power of neural networks with the

* Corresponding author.

E-mail address: yasser.mahmoudi@manchester.ac.uk (Y. Mahmoudi).

| Nomenclature | |
|----------------------------|--|
| Abbreviations | |
| API | Application programming interface |
| CFD | Computational Fluid Dynamics |
| CNN | Convolutional neural network |
| ML | Machine learning |
| NN | Neural network |
| PIMLAF | Physics-informed machine learning-aided framework |
| PINN | Physics-informed neural networks |
| Tanh | Hyperbolic tangent (activation function) |
| XPINN | eXtended (domain-decomposed) PINN |
| <i>Bo</i> | Bond number – ratio defining the effects of gravity to surface tension $\Delta\rho g L^2/\sigma$ |
| <i>Cp</i> | Specific heat capacity [J/(kg·K)] |
| <i>D</i> | Diameter [m] |
| <i>Er</i> | $[(\hat{\Phi} - \Phi)/\Phi] \times 100$ Percentage Error |
| <i>Fr</i> | Froude number ($U_{ref}/\sqrt{g L_{characteristic}}$) |
| <i>g</i> | Gravitational force [m/s ²] |
| <i>L</i> | Characteristic length [m] |
| MSE | Mean-squared error $\left(\frac{1}{n} \sum_{i=1}^n (Y_i - \hat{Y}_i)^2\right)$ |
| <i>p</i> | Pressure [Pa] |
| <i>p_{dynamic}</i> | Dynamic pressure (ρu^2) [Pa] |
| <i>Pr</i> | Prandtl number; ($C_{p,mix}\mu/\lambda$) |
| <i>Re</i> | Reynolds number |
| <i>Relative error</i> | $[(\hat{\Phi} - \Phi)/\Phi]$ |
| <i>T</i> | Temperature [K] |
| <i>t</i> | Time [s] |
| <i>u</i> | Instantaneous streamwise velocity [m/s] |
| <i>v</i> | Instantaneous spanwise velocity [m/s] |
| u | Instantaneous velocity (vector) [m/s] |
| <i>We</i> | Weber number ($\rho_{ref} U_{ref}^2 L_{characteristic}/\sigma$) |
| <i>x</i> | Length in the streamwise direction [m] |
| <i>y</i> | Length in the spanwise direction [m] |
| Symbols | |
| α | Volume fraction |
| ∇ | Spatial differential (del) |
| κ | Interface curvature |
| ρ^* | Dimensionless density (fluid) |
| σ | Surface tension [N/m] |
| ν | Kinematic viscosity [m ² /s] |
| Φ | Data generated by CFD |
| $\hat{\Phi}$ | Data predicted by PINN |
| Subscript | |
| <i>b</i> | Bubble |
| bulk | $(T - T_c)/(T_h - T_c)$ |
| <i>c</i> | Cold |
| <i>CM</i> | Centre of Mass position |
| inlet | Parameter property at the inlet |
| <i>h</i> | Hot |
| <i>ref</i> | Pre-determined reference value |
| <i>T</i> | Temperature |
| Superscript | |
| * | Dimensionless parameter |
| <i>T</i> | Transpose |
| $\hat{\cdot}$ | Predicted data by PINN |

principles of physics to learn and approximate the underlying governing equations of a system [9]. By training on available data and incorporating physical laws, PINNs offer the potential to accurately capture the complex physics of rising bubbles in a reliable and trustworthy methodology which uncovers the traditional ‘black box’ of Machine Learning (ML) tools. While the application of PINNs has been successful in various fields, such as numerical and experimental fluid dynamics [10] and materials science [11], their potential for investigating the multiphysics problem of rising bubbles with heat transfer remains unexplored. This uncharted territory presents an exciting opportunity for future research to leverage the capabilities of PINNs in understanding and predicting the behaviour of two-phase flow in rising bubbles.

While the current PINN formulation has shown promise in problems devoid of multiphysics behaviour, there remains a lack of comprehensive investigation in the literature. Thus, the application of PINNs in solving heat transfer problems involving multiple phases is explored in the present paper. The field of physics-informed neural networks has generated significant interest following the work conducted by Raissi et al. [12]. Their discovery that PINNs could exhibit agnosticism towards geometric and initial boundary conditions has revolutionized the field. This was exemplified by their successful flow predictions over two and three-dimensional cylinders, as well as around a three-dimensional aneurysm [13]. Today, physics-informed neural networks are widely utilized in numerical modelling. Pioch et al. [14] have successfully employed PINNs to achieve the precise reconstruction of recirculating flow over a backward step, a well-known problem in the field of fluid dynamics. Utilising the power of PINNs, they accurately captured the intricate behaviour of the fluid flow, highlighting the effectiveness of this approach in tackling challenging fluid dynamics scenarios. In a study conducted by Jin et al. [15], the effectiveness of PINNs in simulating turbulence was demonstrated. The results revealed a notable

agreement between the simulation results obtained through PINNs and those from direct numerical simulation (DNS). This finding highlights the potential and applicability of PINNs as a reliable tool for accurately capturing turbulence phenomena. The versatility of PINNs extends beyond numerical fluid mechanics, as showcased by Cai et al. [16], who combined the Boussinesq approximation with tomographic background-orientated Schlieren (Tomo-BOS) image data to measure fluid density surrounding a hot cup of espresso. PINNs have also found utility in the field of materials research. Zhu et al. [17] successfully modelled weld pool dynamics using a combination of experimental and computational data, while Niaki et al. [18] analysed conductive heat transfer and resin cure kinetics to provide real-time simulations. As a novel technique, questions remain regarding best practices for using PINNs for fluid flows. However, researchers are intent on closing this gap in knowledge. Addressing the challenges of hyperparameter tuning, Papadopoulos et al. [19] introduced Bayesian optimization to calculate thermal resistance in composite materials. Laubscher [20] explored the effectiveness of segregated neural networks for single-phase channel flows including heat transfer, demonstrating improved results when compared to a combined network architecture. Royer et al. [21] confirmed the efficacy of training optimization for radiative heat transfer problems, extending the accuracy of predictions beyond the training data. As a result, there is alignment amongst the literature that PINN has the potential as a suitable investigative tool where multiphysics is involved and especially useful where data is sparse [22].

Despite these advancements, comprehensive investigations of complex multiphase flows using data-driven PINN methods are still limited. Buhendwa et al. [23] studied rising bubbles to explore the significance of weighting losses and activation functions. Qiu et al. [24] extended this research by incorporating the Cahn-Hilliard approximation to determine the position of a rising bubble with a large density ratio

compared to the domain fluid. Zhai et al. [25] even delved into flows involving multiple bubbles using data-driven PINN methods. However, a research gap exists in the literature regarding the application of PINNs to solve multiphysics heat transfer problems involving multiple phases. Thus, the present paper aims to fill this gap by investigating the application of PINNs in such scenarios, offering insights and advancements in the field of multiphase heat transfer. Additionally, this paper examines the effectiveness of PINN as an extrapolative model for two-phase flows.

To bridge the gap in existing research, this work extends the capabilities of the PINN methodology by incorporating the co-dependant effects of thermal and hydrodynamic boundary layers, flow separation, vortical wakes, buoyancy, and deforming interfaces. To begin, these phenomena are studied independently through four initial case studies: flow over a heated cylinder, single-phase channel flow with temperature, two-phase immiscible channel flow, and isothermal rising bubble. By dissecting and understanding the behaviour of each phenomenon, the predictive capabilities of the PINN technique can be enhanced. The algorithm is tested extensively by modelling extrapolated behaviours due to differing properties and by inferring unobserved fields where applicable. Subsequently, the lessons learned from these independent cases are combined to assess the accuracy of predictions in scenarios involving dependant interactions. Specifically, we focus on the behaviour of a rising bubble with a hot wall, which incorporates the intricacies of multiple interacting phenomena. Our analysis delves into the implications of explicitly imposed boundary conditions, the requisite data for the PINN method, and the impact of network architecture. This paper makes a substantial contribution to the field by systematically assessing the performance of Physics-Informed Neural Networks (PINNs) in handling multiphase problems across three distinct applications: forward problems, inverse problems, and extrapolative problems. This work also expands the application of PINNs to encompass heat transfer problems with multiple phases. Through detailed examinations and insightful analyses, light is shed on the importance of explicitly considering co-dependant effects and valuable insights are provided for future research in this area.

2. Computational methodology

This section provides an overview of the PINN architecture and its corresponding settings. Additionally, the partial differential equations (PDEs) addressed by the solver are introduced, accompanied by a concise discussion on the computational resources necessary for training.

2.1. Governing equations

Fluid behaviour in various scenarios can be comprehensively described by a set of simultaneous partial differential equations (PDEs) that need to be solved [23]. In the most intricate cases investigated in this study, up to five distinct PDEs were simultaneously addressed. These encompass the following:

Mass conservation,

$$\frac{\partial \alpha}{\partial t^*} + \mathbf{u}^* \cdot \nabla^* \alpha = 0 \quad (1)$$

Momentum transport via the incompressible Navier-Stokes equations,

$$\begin{aligned} \rho^* \left(\frac{\partial \mathbf{u}^*}{\partial t^*} + (\mathbf{u}^* \cdot \nabla^*) \mathbf{u}^* \right) + \nabla^* p^* - \nabla^* \cdot \frac{1}{Re} (\nabla^* \cdot \mathbf{u}^* + \nabla^* \cdot \mathbf{u}^{*T}) - \frac{1}{We} \kappa \nabla^* \alpha \\ - \rho^* \frac{1}{Fr^2} = 0 \end{aligned} \quad (2)$$

where,

$$\kappa = -\nabla^* \cdot \frac{\nabla^* \alpha}{|\nabla^* \alpha|} \quad (3)$$

$$Fr = \frac{U_{ref}}{\sqrt{g} L_{characteristic}} \quad (4)$$

$$We = \frac{\rho_{ref} U_{ref}^2 L_{characteristic}}{\sigma} \quad (5)$$

Finally, energy conservation was applied using the transient heat equation:

$$\mathbf{u}^* \cdot \nabla^* T^* + \frac{\dot{q}}{k} - \frac{1}{PrRe} \nabla^{*2} T^* = 0 \quad (6)$$

The Volume-of-Fluid (VOF) methodology, introduced by Hirt & Nichols [26], uses volume fraction (α) to represent the fluid volume fraction in each computational cell. Fluids 1 and 2 correspond to $\alpha = 0$ and $\alpha = 1$, respectively. Advection by local velocities causes the initial volume fraction to change over time and thus it becomes a key parameter in the conservation of momentum. The PINN code deals with phenomena of two-phase interfaces, buoyancy and surface tension using the terms defined in Eqs. (3–5). These relevant PDEs have been encoded into the PINN developed in this work.

2.2. Physics-informed neural networks methodology

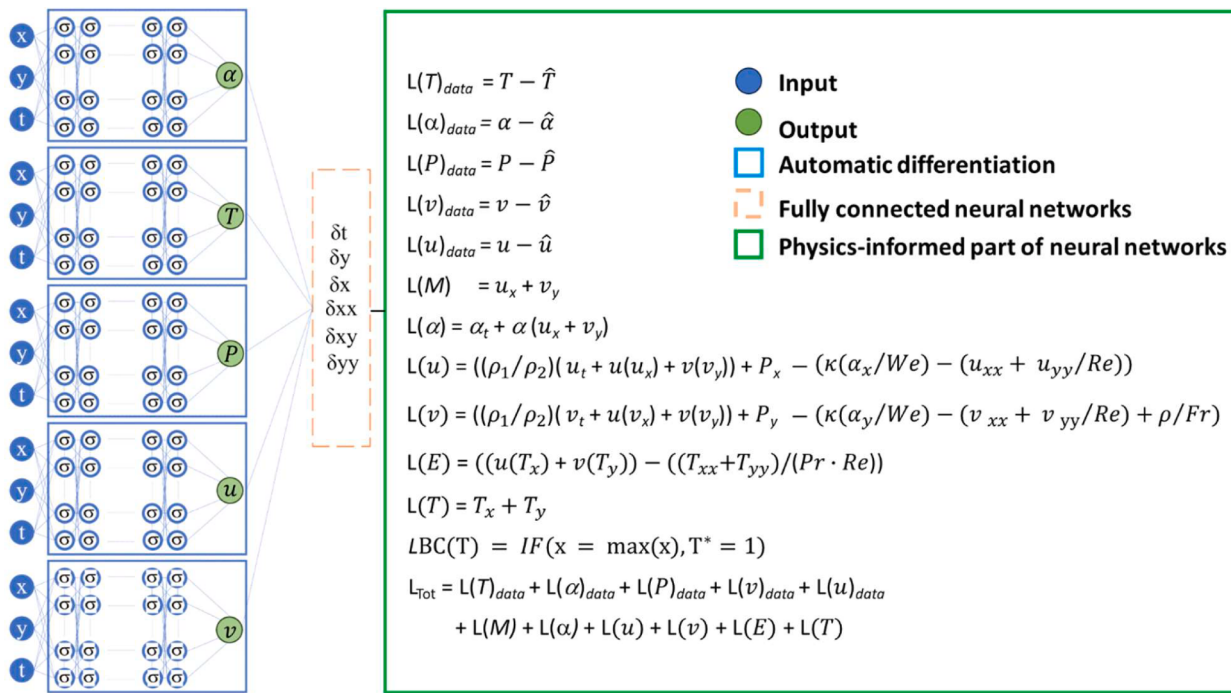
Once the governing equations are known, they can be combined with the initial and boundary conditions to form physics-based loss functions (Eq. (7)):

$$(\mathbf{u}, v, p, \alpha, T) = F_{NN}(x, y, t, \Theta) \quad (7)$$

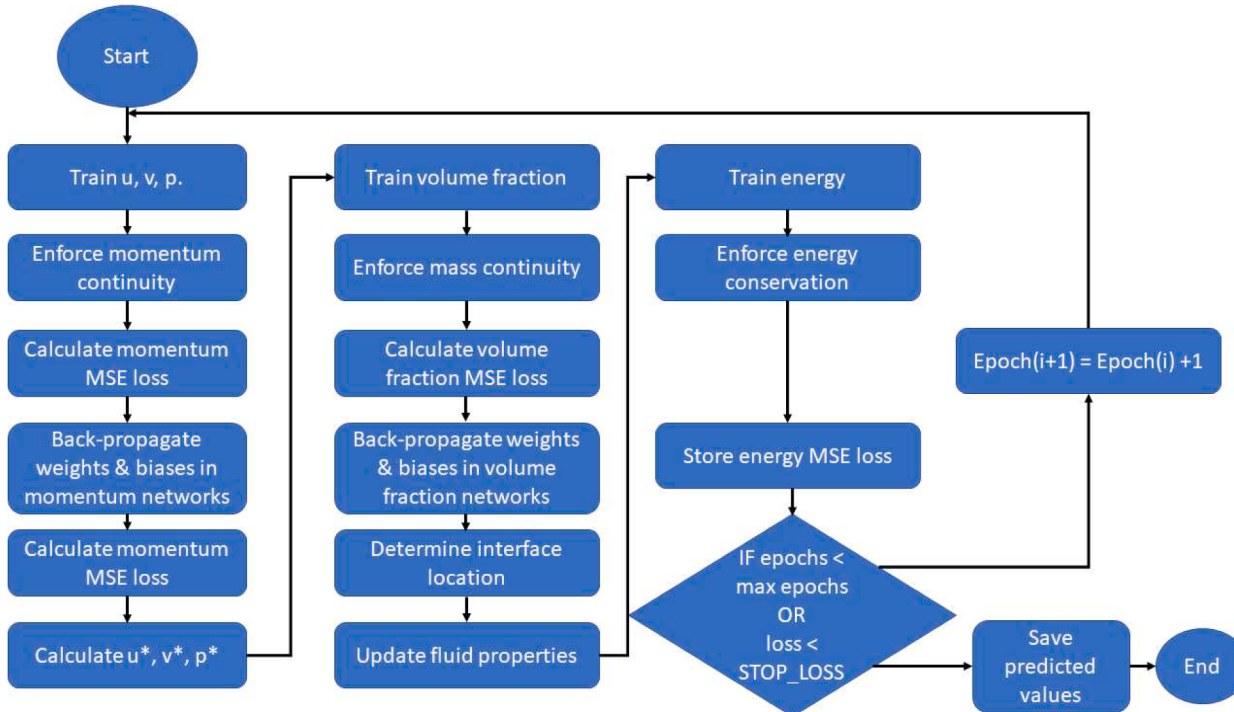
where, F_{NN} represents the total contributions of the individual neural networks, shaped by the trainable parameters Θ of weights W and biases B . In certain cases, complexity demands an additional trainable nodewise coefficient a . As the solver is optimised, the loss terms reduce, and the fully connected networks determine a relationship between the spatiotemporal coordinates (x, y, t) and physical quantities of interest (velocities, pressure, volume fraction and temperature). Each of these variables trains on independent networks (Fig. 1(a)) but the outputs are intertwined such that an accurate output for any given variable is dependant on all other variables being accurately predicted. Where flow complexity demands, nodewise adaptive coefficients are employed to effectively transfer optimisation to a nodal level [27], rather than across the global network. During training, each node experiences a unique landscape and the adaptive coefficients mean that each node must only be optimised for its own landscape, rather than that of the entire network. Though adaptive coefficients induce a computational cost, this is effectively paid back by reducing the total complexity of network architecture, the training epoch window, or both.

In PINNs, the total loss is a composition of individual residual terms from the governing equations losses as well as losses calculated by comparing observed data at certain colocation points to corresponding predictions. In this study, the MSE of the individual residuals is added to calculate the total system loss. Each case study in this work includes a hyperparameter search to ensure the PINN could effectively optimise all components of the loss functions. The results of these searches are included in Table 1. Batch size appeared to play a deterministic role in solution accuracy, in agreement with the literature [28]. Each network relies on the Adam optimiser [29]. Computational expense is defined by core hours (number of cores \times number of hours). It ranged between 16 core hours to around 700 for the channel flow case to the rising bubble with hot wall case, respectively.

Deep learning techniques are extremely sensitive to the design of their networks. PINN is no exception; hence, each case study required some level of hyperparameter tuning to create efficient and capable



(a) The rising bubble with a hot wall case used 5 fully connected neural networks. True properties are shown in Table 1, but for representation purposes, each network displays 4 layers and 4 neurons per hidden layer. All derivatives are computed using automatic differentiation. Each loss term ‘L’ is converted to an MSE value. The sum of these MSE values (L_{Tot}) gives the total loss to be optimised

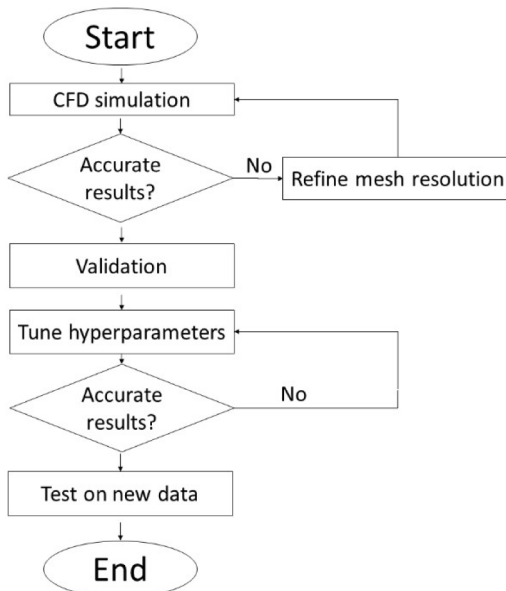


(b) Sequential training strategy for PINN

Fig. 1. Configuration and training strategy of the PINN algorithm; (a) network architecture; (b) training strategy; (c) validation and testing process.

models. The process is described in Fig. 1(c). In this approach, a lower-resolution dataset is supplied to the PINN to train and tune hyperparameters through a coarse-grid search [20]. The inspiration behind

supplying a reduced-density dataset for validation is the work performed in [16], where a synthetic 2D dataset was used to tune a PINN which was eventually applied to a 3D experimental problem. A summary



(c) Validation and testing process for PINN

Fig. 1. (continued).

Table 1
Network architecture for chosen cases.

| Case | Nodes | Layers | Activation function | Number of networks | Batch size | Epochs |
|----------------------------------|-------|--------|---------------------|--------------------|------------|--------|
| Two-phase channel flow | 50 | 10 | 'tanh' | 4 | 2742 | 10,000 |
| Isothermal rising bubble | 150 | 8 | Nodewise 'tanh' | 4 | 265 | 25,000 |
| Rising bubble with heat transfer | 150 | 8 | Nodewise 'tanh' | 5 | 265 | 25,000 |

of important architectural parameters is contained in Table 1.

3. Overview of test cases and numerical settings

The rising bubble with a hot wall problem is multi-faceted, so several case studies were used to isolate the necessary traits for an accurate prediction. To analyse PINN abilities to infer wake behaviour, flow around a cylinder was studied. The energy equation implementation was evaluated using a channel flow case. The prediction accuracy of a two-fluid interface was preliminary assessed using a two-phase channel flow case before complexity was increased to account for buoyancy with rising bubble studies. The initial and relevant boundary conditions of the chosen case studies are represented by schematics in Fig. 2. The physical importance of each of these cases is explained in the ensuing subsections.

3.1. Validation of CFD data

In this work, predictions made by the PINN methodology were informed by CFD data. Comparisons were also made between the PINN predictions and the CFD results. However, it is important to ensure that the provided training data from CFD are validated against benchmark data from literature. It was particularly important to verify the present

work CFD data for two-phase problems, where analytical solutions are difficult to obtain [27]. Hence, the present CFD data were compared against benchmarking data from Hysing et al. [27]. Fig. 3(a) and 3(b) revealed a maximum discrepancy of less than 1% for both the centre of mass position and the bubble rise velocity, respectively. Consequently, the present CFD data were verified to be used as training data for the PINN methodology in this study.

3.2. Single-phase cases

To assess the capabilities of PINN, it was advantageous to consolidate findings in single-phase flows which accommodate desirable phenomena, including wake flow (occurs behind the rising bubble) and the development of thermal and hydrodynamic boundary layers caused by bubble motion against the hot wall. As such, the developed PINN model has been used to predict (i) the evolution of wake vortices behind a heated cylinder and (ii) thermal and hydrodynamic boundary layers in a channel flow with heated walls. Geometries and boundary conditions can be seen in Fig. 2(a,b), while further details of these cases can be found in the appendix.

3.3. Two-phase immiscible channel flow case

To evaluate the accuracy and perceived sharpness of PINN-predicted two-phase interfaces, a two-phase immiscible channel case (with a flow Reynolds number of 100) was constructed, based on the work of Laubscher [20]. In this case, the fluid interface was produced from inference alone, drawing parallels to the rising bubble cases where it may be impractical to specify the boundaries of the bubble over time. Cases where two immiscible fluids flow in parallel represent a challenge to the resolution of the fluid interface. The confinement of scalars within a narrow window gives rise to sharp gradients of the colour function (scalar concentration values) on the approach to the interface, which may cause a diffused solution if treated incorrectly. In real terms, this may translate to a thicker interface being predicted than would be seen under experimental conditions. The accuracy of interface construction was tested for a two-fluid channel flow case. In this case, the two fluids were differentiated solely by their viscosities ($\nu_1 = 0.01 \text{ N/m}$ and $\nu_2 =$

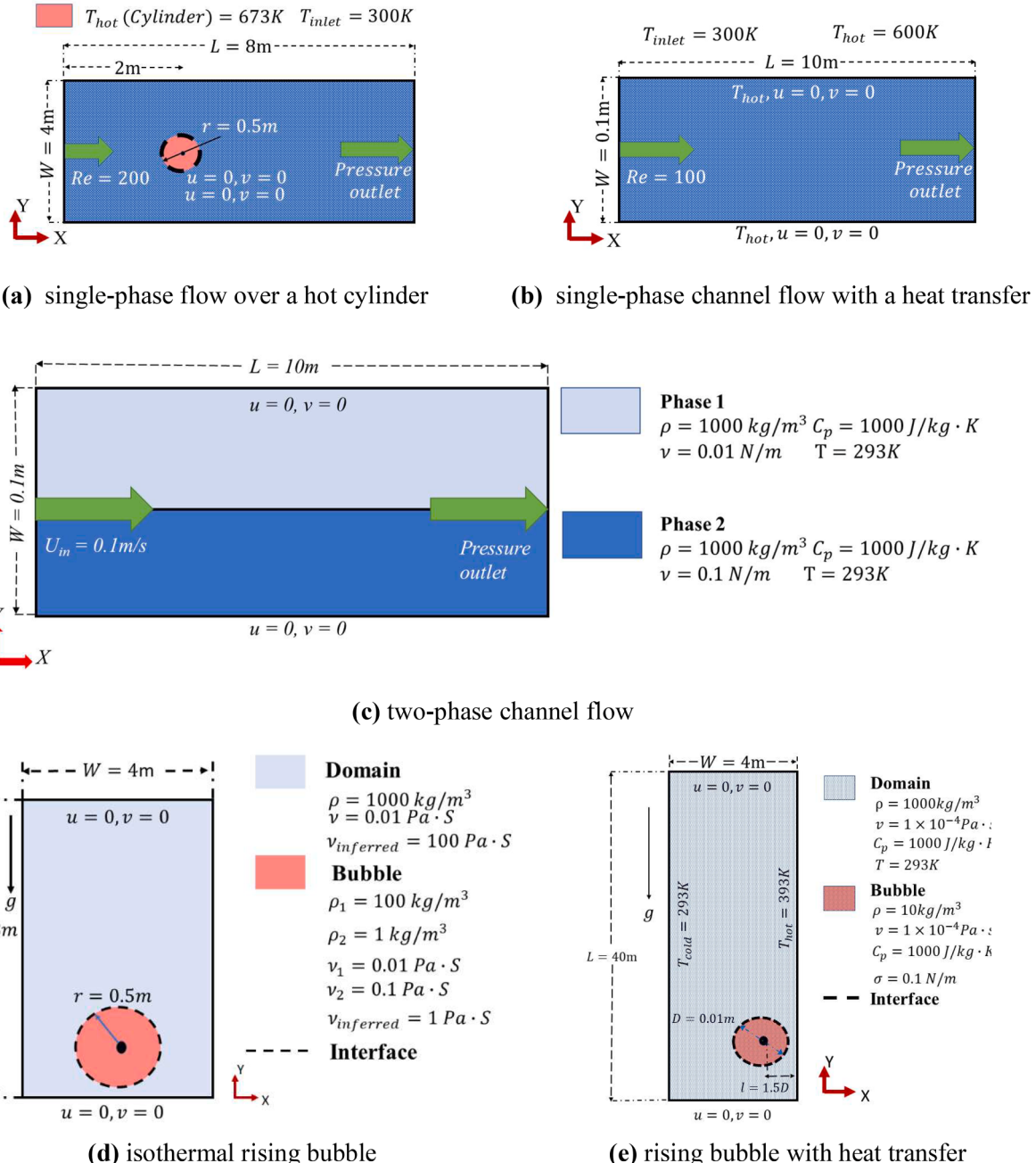


Fig. 2. Setup for chosen case studies (a) for single phase flow over a hot cylinder, (b) single-phase channel flow with heat transfer, (c) two-phase channel flow [20], (d) isothermal rising bubble [23], and (e) rising bubble with heat transfer [37].

0.1 N/m). The configuration imposed an initial interface at the vertical mid-point of the channel and constrained the fluids by a non-slip condition at the north and south boundaries. A linear velocity inlet was prescribed, though the differing viscosity caused a Poiseuille-like behaviour [23] along the length of the channel (see Fig. 2(c)). Due to the fluid properties, there was no need to implement and validate a gravitational source term. Thus, the complexities of buoyancy could be eliminated. The definition of success for this problem was based on two criteria. The first was the constraint of the volume fraction prediction entirely between 0 and 1 for the full domain. The second was for the position of the interface to match that of the CFD simulation data.

3.4. Isothermal rising bubble case

To begin to determine the veracity of PINN predictions concerning co-dependant physical phenomena, it was necessary to study a rising bubble. A single rising bubble is a common test case for interface solvers because it brings together the effects of buoyancy and surface tension, which have significant impacts on the position and shape of the interface [31]. These test cases each concern a single bubble in a liquid column, undergoing interfacial deformation and evolution. It was important for the progression of the rising bubble with a hot wall case that the PINN method could maintain a sharp interface once the fluid properties were considered. It provides a thorough assessment of how PINN copes with additional complexity before considering the effects of a convection cell. In the first case (hereby known as ‘ellipsoid’), the bubble underwent a

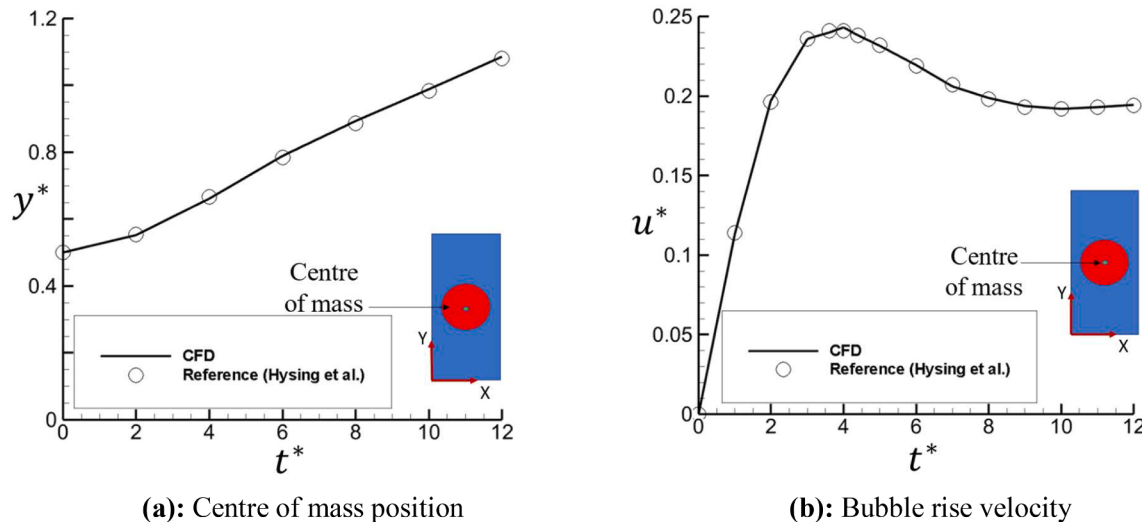


Fig. 3. Comparison of ellipsoidal isothermal rising bubble CFD data produced for this study, including (a) centre of mass position and (b) bubble rise velocity, compared to reference data by Hysing et al. [30].

moderate interfacial deformation [32]. In the second case (hereby known as ‘skirted’), deformation was much more pronounced and tended towards bubble breakup. In both cases, results comprise a mixture of qualitative (for the interfacial shape) and quantitative analysis (centre of mass and velocities), respectively.

These case studies relied on differing material properties to provide observations of alternative direct topological behaviours of interfacial deformation as well as pertinent indirect topological measurements such as velocity and pressure (refer to Table 1 for network parameters). In both simulations, the fluid domain was quiescent. It remained so throughout the simulation, but for motion caused by the rise of the bubble. In these cases, the bubble motion was therefore not reliant on some imposed velocities at the domain boundaries. Any motion was solely dependant on the effects of buoyancy. For these rising bubble case studies without heat transfer, the thermophysical properties are the same in both cases except for kinematic viscosity and bubble density. Properties are shown in Fig. 2(d).

In the ellipsoidal and skirted isothermal rising bubble case studies, training data comprises 75% of available CFD data (from 60 CFD timesteps). The remaining 25% of the training data timesteps were reserved for testing purposes. Therefore, PINN predictions in the vicinities of these times were based purely on learned physics. An extended hyperparameter search was performed in this case. A 150-node by the 8-layer network was revealed to be the most acceptable compromise of accuracy and computational demand. Obtaining accurate solutions in all the rising bubble cases (with and without heat transfer), required the use of locally adaptive activation functions in conjunction with adaptive weights. In these cases, a stepped learning rate was employed, decreasing every 5000 epochs. The learning rates were as follows: 1×10^{-4} , 5×10^{-5} , 1×10^{-5} , 5×10^{-6} and 1×10^{-6} . The ellipsoid case served as a proof of concept to test the additions (surface tension and buoyancy) to the solver, while limiting the complexities of vastly different fluid properties as explained in [23]. The skirted case validated these findings on properties more closely aligned to those targeted in future boiling studies.

3.5. Inferred isothermal rising bubbles

It is essential for practical application of PINNs that they provide a demonstrable advantage over traditional CFD methods. It is known for single forward problems PINN is slower than CFD methods [33,34]. Therefore, this advantage translates to the ability to provide accurate information where significantly less data is available for training, either

due to incomplete measurements of a given field or by making predictions based on properties beyond the range of observed data. To this end, the detailed methodology has been applied to two isothermal rising bubble problems which rely on significantly more inference to predict bubble behaviour.

One approach to demonstrating the inverse abilities of the algorithm is to use the solver to predict follow methodology used by Buhendwa et al. [23] which uses observed data in complimentary fields to determine the behaviour of an unobserved field. In real systems, the measurement of auxiliary fields such as interface position can often be easier compared to visualisation of the entire velocity or pressure fields. In such cases, PINN can assist with the reconstruction of these ‘hidden variables’. To evaluate this approach, the network is trained on the ellipsoidal bubble as detailed in Section 3.4. However, only the volume fraction field is continuously provided. The corresponding velocity fields are generated through inference alone. This problem is hereby known as an ‘inferred ellipsoidal’ isothermal rising bubble. Results are presented which further demonstrate that PINN is a useful methodology to infer behaviour when it is not possible to provide high quality measurements.

In the second approach to inverse modelling applications, the model is used to predict the behaviour of a bubble whose fluid properties differ from previously observed data. This follows a second definition of ‘inverse’ problem, as defined by Lonher et al. [35]. Since there is no training data with properties close to the target values, predictions rely on minimising the error only through solving the PDE equations, rather than the previous approach of using a combination of minimising error against observed data and making physics-informed predictions simultaneously. This bubble, hereby known as a ‘spherical cap’ rising bubble [36] takes its name from its flat underside and convex top half (Fig. 4). The necessary Bond and Reynolds numbers to achieve a spherical cap bubble [37] (22.5 and 50, respectively) reveal that this is an extrapolative application of the inverse PINN modelling strategy. Initial conditions are displayed in Fig. 2(d). According to an additional literature survey [38–40], extrapolation is a significantly more demanding task than interpolative mapping for neural networks. Therefore, achieving acceptable results using extrapolative means indicate even better results are achievable for interpolative models. Bond and Reynolds numbers are displayed for several bubble topologies. Ellipsoidal and skirted topologies have a Reynolds number of 35 and vary in Bond number. An extrapolative test case to model a spherical cap bubble is performed, where the Reynolds number is higher than that observed in the training data.

To obtain the predictions for the spherical cap bubble, a combined

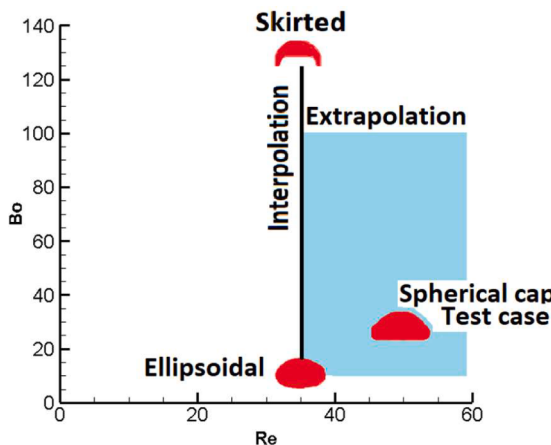


Fig. 4. Bond (Bo) and Reynolds (Re) numbers required to produce various bubble topologies observed in this work. Only bubbles with $Re = 35$ are provided for training. Data to produce this map is taken from [5].

weight set is created by using outputs from the ellipsoidal case then by training on skirted bubble data for 5000 epochs. Finally, the PINN is trained on the properties of the spherical cap bubble for 1000 epochs at a large learning rate (1×10^{-4}). Results of the extrapolated prediction are compared against CFD data.

3.6. Rising bubble with a hot wall

The final case in this study was a true assessment of PINN predictions for multiphysics flows, combining all the physics seen in the single rising bubble case with convection flows within the domain. A single bubble rising near a hot wall is a case of great interest in the heat transfer community because it is a precursor to boiling heat transfer [41–43]. Under such conditions, the shape and position of the bubble have dramatic effects on the heat transfer within a system because of the ensuing wake region. Maeng and Park [44] discussed the impact on heat transfer of wake vorticities of an oblate bubble moving in a zig-zag motion. The wake vortex pairs observed in this setup impact the wall and move upwards slowly. A small amount of bulk liquid is entrained towards the wall as a result, increasing the local Nusselt number. Each vortex pair arrives at the wall in sequence, forcing a sustained wall-wake flow interaction. The overall impact of this is a drop in local wall temperature within the entire wake region.

The geometry for the CFD setup was based on work by Larimi and Ramiar [45]. The properties of the simulation are shown in Fig. 2(e). In this study, a bubble rose in a quiescent liquid which filled the domain. Initially, the bubble was positioned at $1.5D$ from the hot wall and $8D$ from the base of the vertical channel. The VOF model used here has been validated by Deen and Kuipers [46] who performed a numerical simulation of gas bubbles rising within viscous liquids. The initial temperature condition for this study was taken as a linear profile in the x -direction, $T(x) = (T_h - T_c)(x/L) + T_c$, where T_h and T_c are the temperatures of the hot and cold walls, respectively. Over time, this condition changed due to natural convection within the vertical channel.

The CFD contained 26,321 cells (PINN collocation points at cell centres). The rising bubble cases utilised meshes on the order of ten times as dense as the simple single-phase channel flow case and over three times as dense as the cylinder flow case. There is certainly scope for increasingly sparse training data in future works, but as this study was billed as a proof of concept, a complete study on the density of collocation points was not performed. Hyperparameters used in this case mirrored those used in the isothermal rising bubble case studies including learning rates of 1×10^{-4} , 5×10^{-5} , 1×10^{-5} , 5×10^{-6} and 1×10^{-6} . In this study, 50% of the CFD timesteps were reserved and used for testing. This represents a significant increase in learned physics

compared to the traditional split of training and testing data of 80% - 20%. At the tested timesteps, the PINN made predictions based on the physics it learnt. Both nodewise activation functions and adaptive weights were used in this study based on the improved accuracy observed in the rising bubble ‘ellipsoid’ study. Likewise, parameters were chosen based on lessons learnt as part of the rising bubble cases without heat transfer. A thermal boundary condition on the right-hand wall was enforced to improve the accuracy of the wake vortex interaction.

4. Results

In this section, results obtained from PINN predictions are presented, focusing on the comparison of key physical phenomena. These include the co-dependant effects of thermal and hydrodynamic boundary layers, flow separation, vortical wakes, buoyancy, and deforming interfaces, as described in the cases discussed in Section 3.

4.1. Single phase cases

The PINN code has achieved positive results in both momentum and heat transfer domains for flow around a cylinder. Figs. 5 and 6 illustrate that the code was able to infer a true representation of fluid behaviour in these domains. The thermal domain undergoes a Von Karman Street vortex, mirroring the momentum field which drives the oscillations. Where the eddies exist, there is less heat transfer because thermal convection is restricted. A similar vortical wake phenomenon is apparent with the skirted bubble case, so it was imperative to accurate flow reconstruction so that the PINN could accurately represent complex flow conditions in future work. Meanwhile, the single-phase channel flow case demonstrated that both thermal and momentum boundary layers were accurately inferred without supplying boundary conditions to the PINN algorithm. This ability is vital for an accurate representation of the thermal and momentum domains for the rising bubble with a hot wall. Further discussion of these results can be found in the appendix.

4.2. Two-phase immiscible channel flow case

In the case of two-phase immiscible channel flow, the PINN method inferred an accurate volume fraction distribution including distortion in the vicinity of $x^* = 2$; an artefact of the differing viscosities within the channel which is supported by the analytical work of Rezavand et al. [31]. Though the PINN-generated interface carries more noise than the CFD counterpart, it made a reliable interpretation of the location and size of the interfacial kink. The noise could be improved by either creating a denser network (more nodes) or supplying more data at the interface, but both carry consequences in terms of training time. As with the CFD model, the PINN predicted the viscous fluid sinks below $y^* = 0.5$, though the initial gradient produced by PINN was slightly shallower. This was deemed inconsequential because in general there was a good agreement between the PINN and CFD results.

Quantitative analysis in Fig. 7(c) indicates a similar level of success. The volume fraction prediction has been constrained between the physical limits of $0 \leq \alpha \leq 1$ in its entirety. In this case, the slight interfacial diffusion throughout the domain served as a source of caution for future work, though it did not detract from the importance of the result achieved. Overall, the analysis of this case gave great confidence that the PINN algorithm is capable of modelling two-phase flows and accurately reconstructing a two-phase interface. This was a vital prerequisite to analysing rising bubbles.

4.3. Isothermal rising bubble case

The exact regime of a rising bubble can be determined using the Reynolds and Bond numbers. An ellipsoidal bubble has a Reynolds and Bond number of around 35 and 10, respectively. A skirted bubble has a

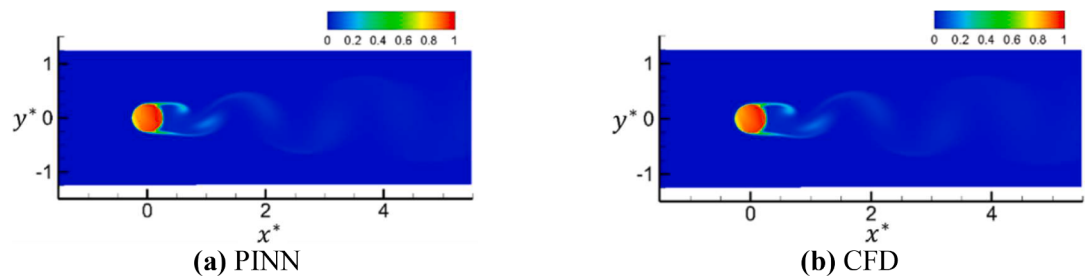


Fig. 5. Comparison of temperature (T^*) between PINN prediction and CFD results for flow over a hot cylinder at $t^* = 15$.

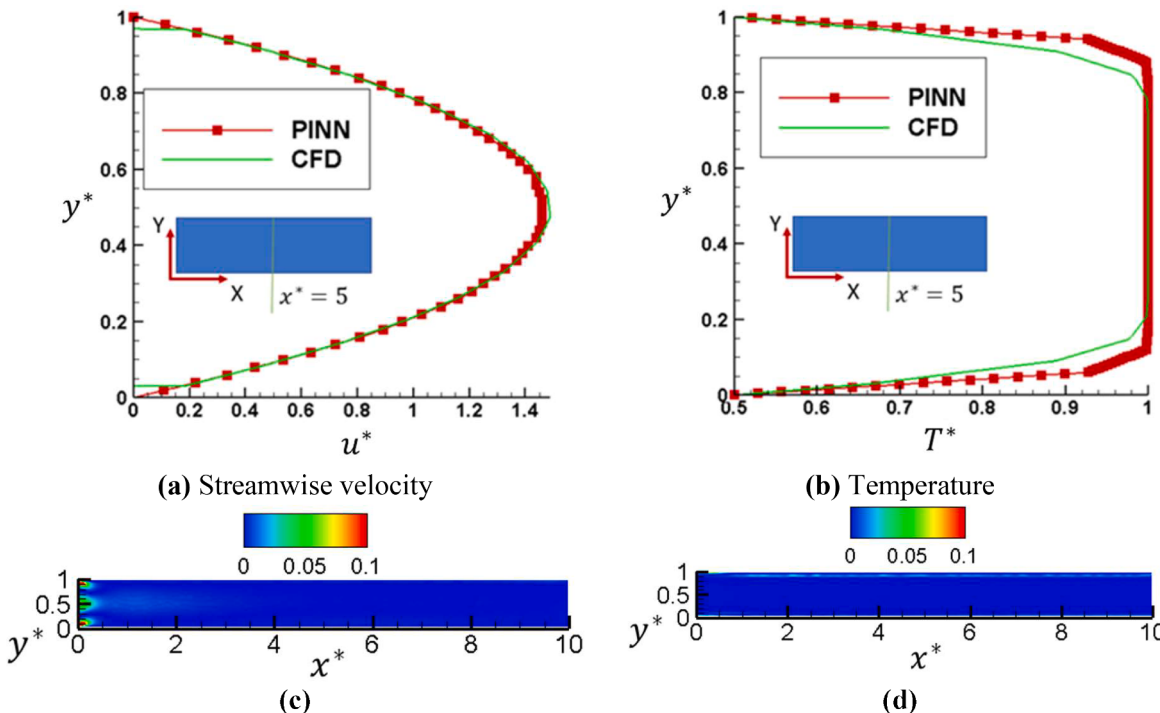


Fig. 6. Comparison between PINN prediction and CFD results at $x^* = 5.0$ for single-phase channel flow case at $t^* = 15$. (c) and (d) show MSE of the u-velocity and temperature fields, respectively.

Reynolds and Bond number of around 35 and 125, respectively [5]. Under both the ellipsoidal and skirted regimes, the bubble maintains a steady rise along a straight path since the wake remains laminar. Results for two-phase rising bubble cases are promising at this stage. At $t^* = 12$, the ML prediction of streamwise velocity shows good agreement with the CFD model. The bubble phase is centred at $y^* = 4.0$ at this point. There are no notable discrepancies, meaning the addition of the Froude term to the Navier-Stokes equations was implemented correctly. Analysis of the volume fraction plot reinforces this by revealing the centre of mass of the bubble phase is tracked extremely accurately, and the predicted height matches the location specified by the CFD data. The largest discrepancy in the centre of mass position (y_{CM}^*) occurred at $t^* = 2$, producing an error ($Er_{CM} = [\widehat{y_{CM}^*} - y_{CM}^*]/y_{CM}^* \times 100$) of 2.8%.

Quantitative analysis of the volume fraction validates that the bubble volume reached roughly the centre of the domain in both cases by the end of the period studied, as confirmed by Fig. 8(a-c). This reiterates the buoyancy term (Froude number) has been accurately implemented in the method. Another key metric which has been satisfied by the PINN methodology is that volume fraction (α) predictions are constrained between the ranges of 0 and 1. Fig. 9 shows comparisons of bubble volume phase fraction at the final timestep ($t^* = 12$). Visually, the two contours exhibit high levels of conformity depicting the interfacial shape of the bubble. In essence, the PINN algorithm accurately located the

interface between the denser fluid ($\alpha = 0$) and the bubble ($\alpha = 1$). The exact distribution of the volume fraction towards the extremities of the bubble produced a mean-squared error of up to 0.25 compared with the CFD exemplar data. Much of the interfacial region resulted in a near-zero error. Two minor areas of concern are the top of the bubble cap and the lower-left side of the bubble. Neither of these discrepancies materially impacted the bubble position or its interfacial shape, however. Currently, PINN predictions cannot represent the sharpest changes in volume fraction. In practice, this means the PINN predicts more granular changes in volume fraction and as such the smallest details are lost when compared to the CFD data. Overall, a visual inspection of Fig. 9(a-c) illustrates highly coherent results between CFD and PINN. Therefore, PINN gave satisfactory results in tracking a rising bubble in the ‘ellipsoid’ setup.

The second case (Fig. 9(d-f)) depicts a skirt bubble formation, realised due to the relatively significant difference in kinematic viscosity between the fluids, typical of water-air interactions. Skirt bubbles can often develop into bubble breakup, so represent a robust assessment for PINN numerical techniques as a precursor to multiple bubble cases. The material properties (see Fig. 2(b)) also pose a major mathematical difficulty for PINN algorithm optimisation. Notably, the ratio of fluid density is larger by a factor of 100 compared to the ellipsoid case, while the surface tension has reduced dramatically ($\sigma = 1.96$ N/m). These

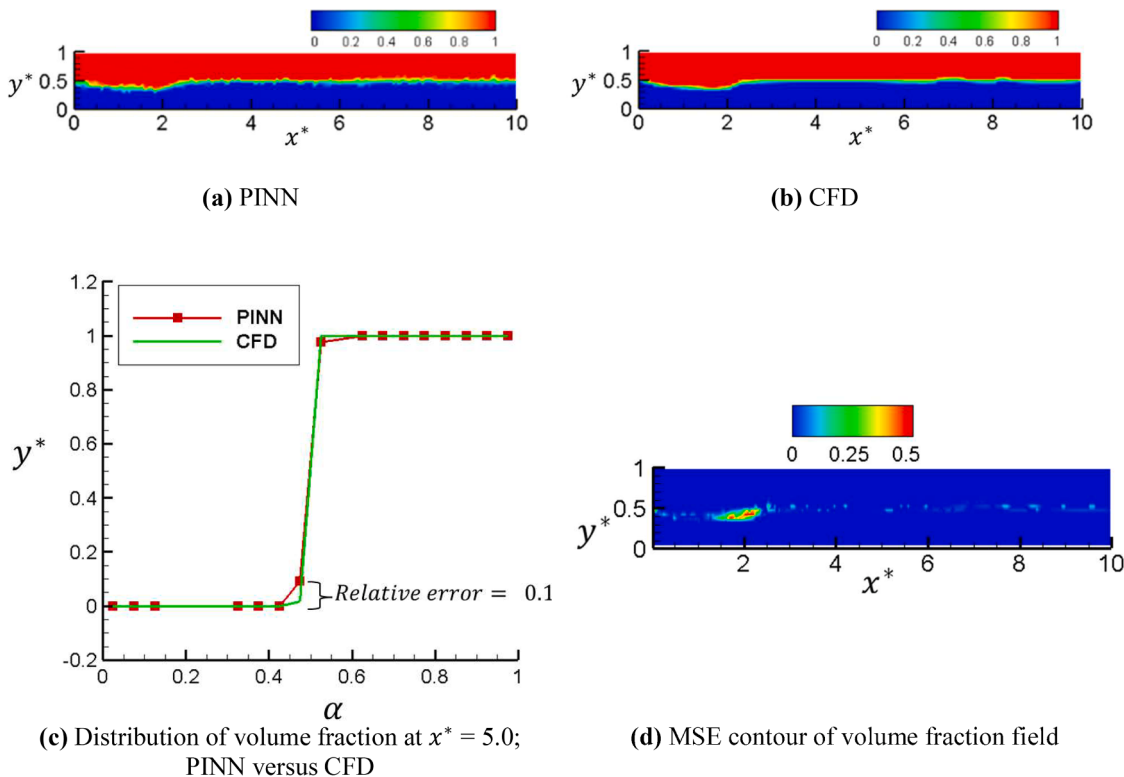


Fig. 7. Comparison between PINN prediction and reference CFD results for isothermal two-phase channel flow case for volume fraction (α) at $t^* = 15$: (a) PINN, (b) CFD, (c) distribution of α predicted by PINN and CFD at $x^* = 5.0$ and (d) MSE contour of volume fraction field.

sharply contrasting fluid properties give rise to filaments on the lower side [30]. The large differences in magnitudes of relevant parameters could pose a limit to training accuracy as explained by Laubscher [20]. Large discrepancies hinder the minimisation of loss values (i.e., successful training). Under circumstances where these large contrasts occur, often the properties with the smallest magnitudes are minimised to an acceptable level but properties with larger magnitudes do not see much improvement. Here, locally adaptive activation functions in conjunction with adaptive weights using the Neural Tangent Kernel (NTK) methodology [47] were implemented to overcome errors caused by these vastly different gradients. The PINN was trained four times to cover the possible combinations of adaptive parameters. It was only when both adaptive weights and nodewise adaptive activation functions were combined that the PINN produced accurate results. The results below demonstrate that the PINN algorithm can model the motion and complex topology of a bubble with large fluid property contrasts to the fluid domain.

Fig. 9(d–f) reveal the PINN methodology has been able to predict the general topology and position of the bubble to a high level of accuracy. Once again, the phase fraction values were constricted between 0 and 1 by the law of mass conservation. Of great interest are the trailing flanges, a major differentiator to the ellipsoid case. The PINN algorithm has successfully captured the general behaviour of these flanges. Analysis of MSE reveals the PINN algorithm correctly predicted the bubble topology, but diffusion in the interfacial prediction resulted in a MSE value approaching 0.3 for the bubble cap and bottom edge. The flanges were well-represented. This indicates that the location of the interfacial regions was predicted to be slightly inaccurate, though not excessively diffused.

Some quantitative analysis (Fig. 10) demonstrates that the centre of mass is tracked accurately for the skirted case. Inferred velocity trends (u^*) are also accurate. As with the ellipsoid case, there was an over-prediction of u^* at $y^* = 4.0$, though it was minuscule compared to the earlier case. Further work on varying Reynolds and Bond numbers will

help explain this increased accuracy and thus PINN limitations.

The qualitative and quantitative results demonstrate that PINN can be successfully applied to capture the position of an interfacial boundary with reasonable accuracy. However, capturing the finest interfacial details requires a network whose density may outweigh the time efficiency benefit offered by a PINN model.

4.4. Inferred isothermal bubbles

In this sub-section, a comprehensive evaluation of the PINN results for inverse modelling and extrapolation prediction is conducted. These results are generated using the methodologies explained in Section 3.5 and are compared to reference CFD outcomes. In Fig. 11, the ability of PINN to accurately infer the velocity field based on the volume fraction field as explained in Section 3.5 is explored. Moreover, Fig. 12 showcases the side-by-side comparison of the spherical cap formation as predicted by both CFD and PINN, offering a clear view of PINN's extrapolation capability. The temporal trajectory of the centre of mass is analysed, providing additional insights into the performance of PINN for extrapolation.

In Fig. 11, the analysis of the inferred ellipsoidal case revealed velocity predictions consistent with the standard ellipsoidal bubble case. Though there is some minor underprediction of the maximum spanwise velocity (Fig. 11(a) and (b)), the streamwise velocity fields (Fig. 11(c) and (d)) show an excellent match. Clearly, minor inaccuracies in spanwise predictions have not translated to errors in streamwise predictions. Succinctly, there is no notable increase in error caused by removing the data comparison opportunities for the velocity fields.

In Fig. 12, despite not providing any data on the spherical cap bubble to the PINN, the shape and trajectory of the bubble have been inferred with a high degree of accuracy. Fig. 12 reveals that inferred behaviour is coherent with CFD data. MSE shown in Fig. 11(c), reveals some interfacial diffusion but generally highly accurate results. Maximum MSE reached 0.27 at a single point in the interfacial region, but the remainder

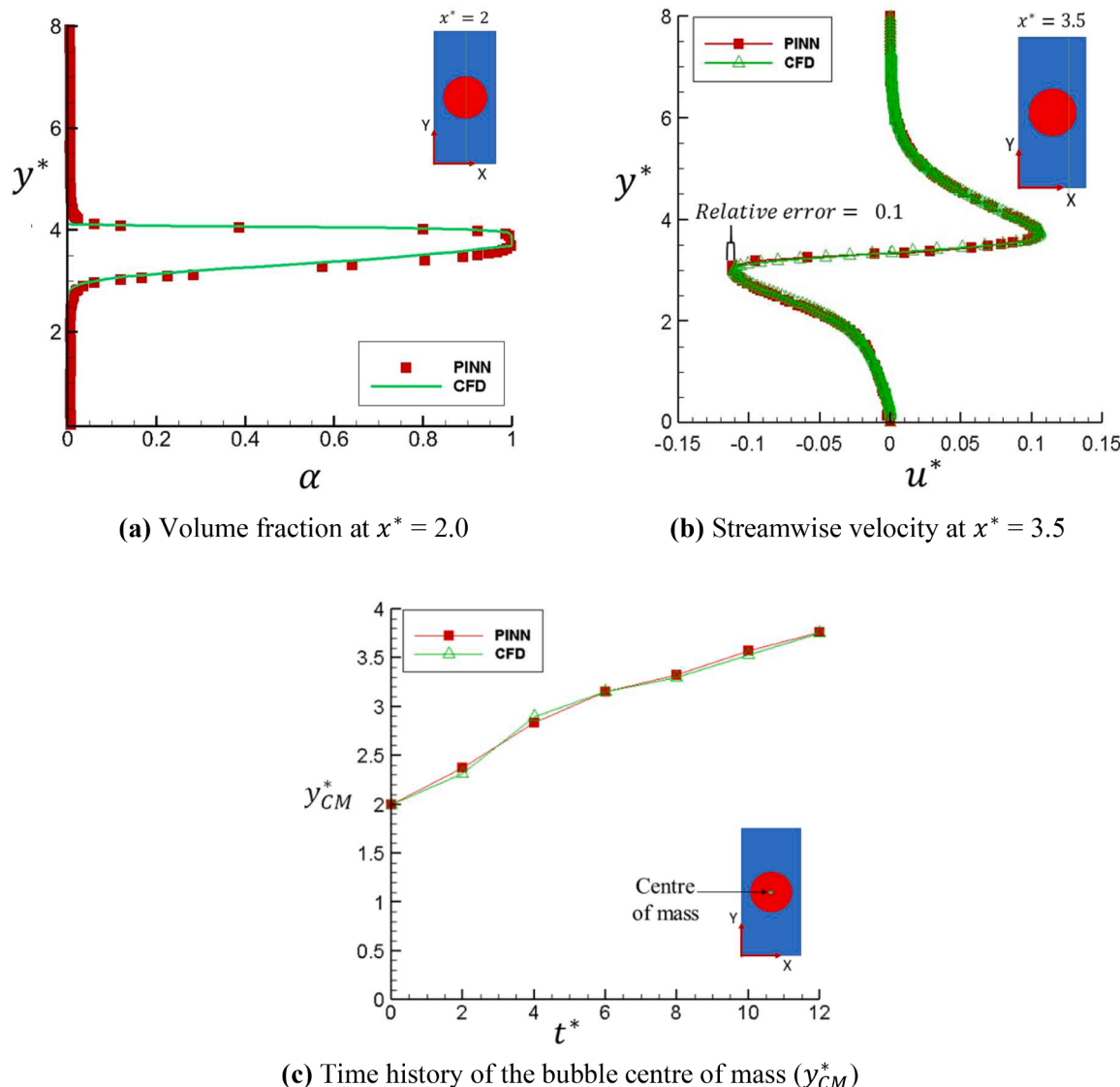


Fig. 8. Comparison of PINN prediction and CFD results for isothermal rising ellipsoidal bubbles: (a) Volume fraction at $t^* = 12$, (b) Streamwise velocity at $t^* = 12$ and (c) Time history of the ellipsoidal bubble centre of mass height. Relative error is defined as $[(u_{CFD}^* - u_{PINN}^*) / u_{CFD}^*]$, which quantifies the relative accuracy of predicted values at a given point.

of the interface was reproduced with a maximum MSE of around 0.08. Analysis of the centre of mass position over time confirmed that the inference was accurate, revealing a maximum discrepancy of 1.3% at $t^* = 8$, which is aligned with the previous isothermal rising bubble cases (Section 4.3). To obtain reasonable results, the network required training using physics alone for an additional 1000 epochs. This accounts for the reduction in maximum error compared to the ellipsoidal case.

4.5. Rising bubble with a hot wall

Two facets were considered when determining the success of this PINN application to a single rising bubble with a hot wall. Namely, tracking the bubble phase and analysing the impact of the bubble wake on wall temperature. Throughout the bubble motion, qualitative analysis of the CFD data shows the bubble volume moving away from the hot (right-hand) wall. By the third quartile of simulation time, the bubble moves back towards the hot wall, demonstrating a clear ‘zig-zag’ motion as observed experimentally by Maeng and Park [44].

Beginning with an analysis of the interface tracking capabilities,

Fig. 13(a–g) illustrates a clear zig-zag behaviour. This occurs due to a combination of the convection currents near the hot wall, which push fluid towards the colder region, and the Reynolds number of the bubble which is large enough to force it into a wavy regime ($Re_b = 750$). The PINN technique used the training data to make a correct representation of the initial state of the bubble. As time progressed, the PINN algorithm did a respectable job of approximating this behaviour; the centre of mass was tracked accurately across the domain as the bubble rose, and the interface did not suffer diffusion. The qualitative analysis shows no additional diffusion in the bubble-domain interface, which proves that the PINN algorithm can predict sharp interfaces. The conjugate effects of convection and buoyancy on the bubble centre of mass are correctly captured, as confirmed by Fig. 13(h). The maximum error of the centre of mass position (Er_{CM}) of 3.6% occurred at $t^* = 32$, but across the rest of the simulation, the error remained below 1%.

Temperature field predictions were studied to determine the accuracy of wake-wall interaction reconstruction. As explained by Maeng & Park [44], the bubble caused a large increase in local Nusselt number since it encouraged motion within the thermal boundary layer. Correspondingly, as the bubble travels upwards within the domain there is a

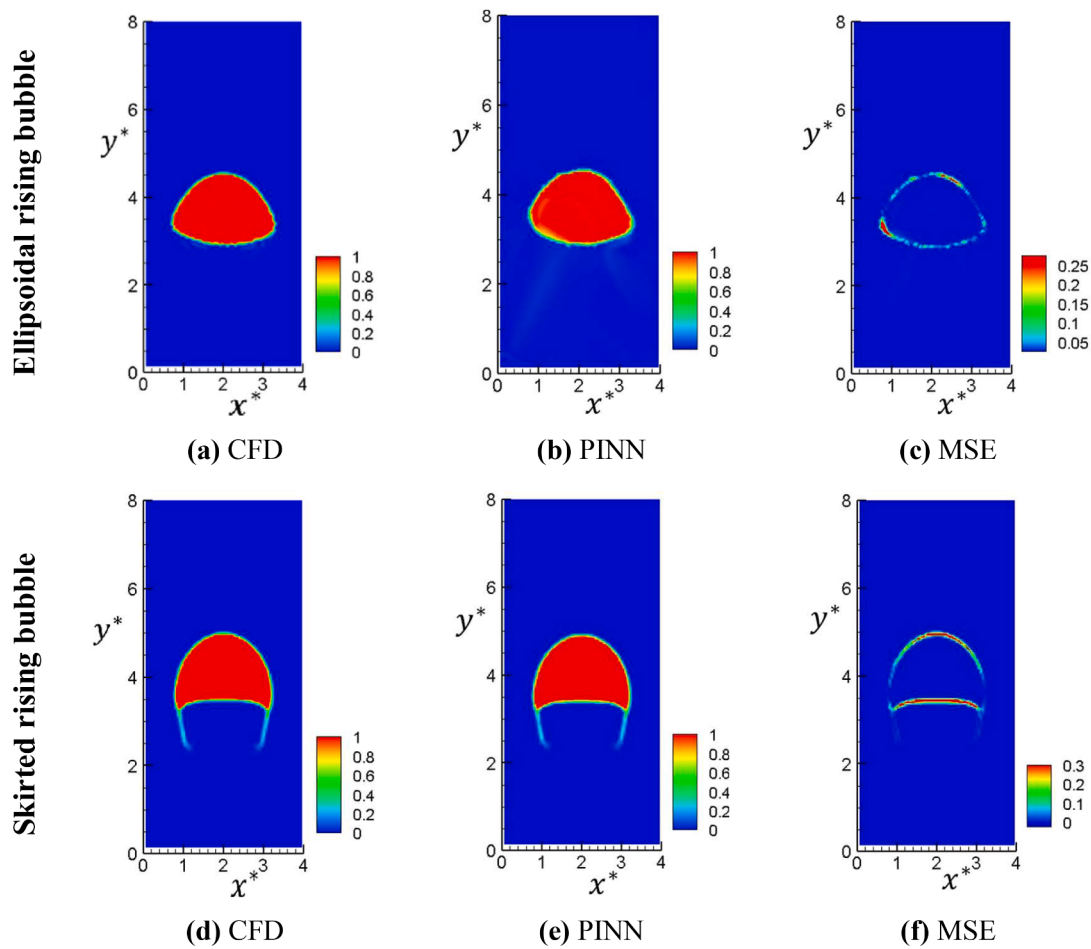


Fig. 9. Comparison of volume fraction between CFD results and PINN prediction with Mean Squared Error (MSE) at $t^* = 12$: Top: Ellipsoidal isothermal rising bubble and Bottom: Skirted isothermal rising bubble.

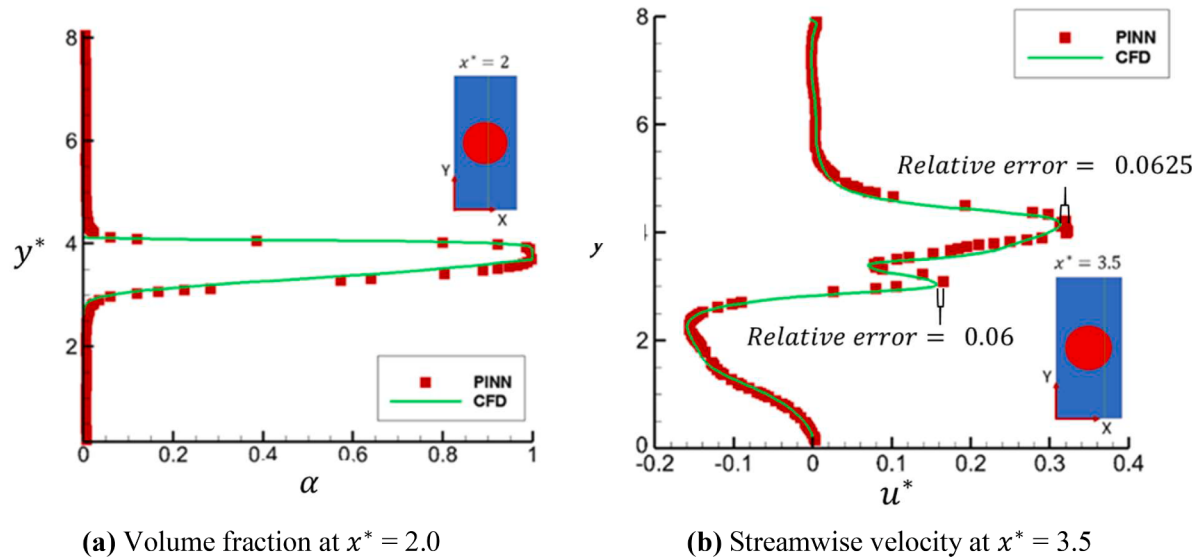


Fig. 10. Skirted rising bubble case analysis at $t^* = 12$ of (a) volume fraction height and (b) streamwise velocity. Relative error is defined as $[(\hat{\Phi} - \Phi)/\Phi]$, which quantifies the accuracy of predicted values at a given point.

notable change in temperature distribution. The thicker thermal boundary layer initiated by the bubble wake is visible in the CFD contours (Fig. 13(a-e)). Comparatively, the PINN code (Fig. 13(f,g)) has

made predictions faithful to the CFD data, with a maximum error ($Er_T = [(\widehat{T}^* - T^*)/T^*] \times 100$) of 1.5% in the bubble wake region. In particular, the entrainment of warmer fluid into the wake region is captured

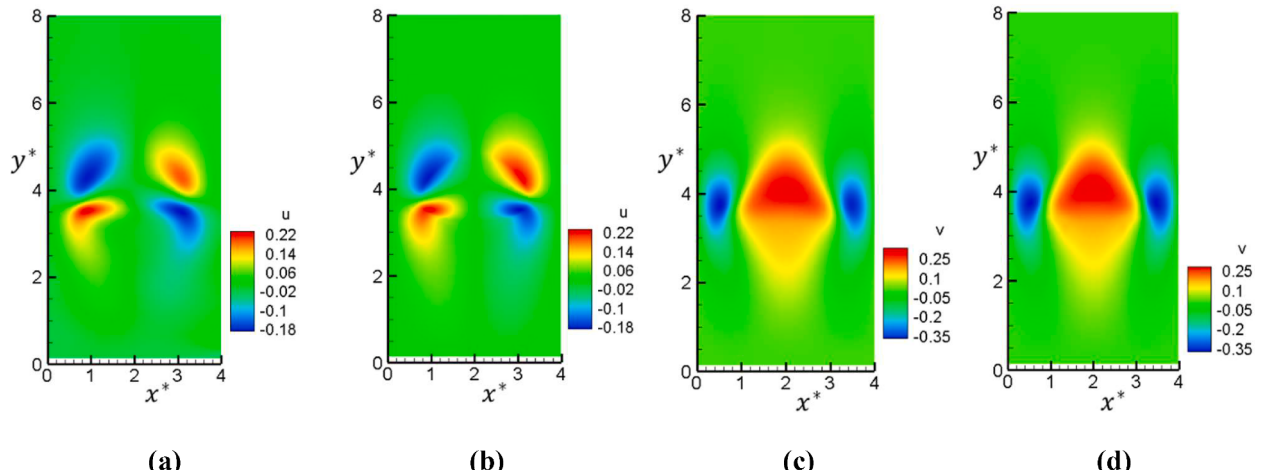


Fig. 11. Comparison of inverse predictions of spanwise and streamwise velocities (a and c, respectively), with CFD reference data (b and d, respectively).

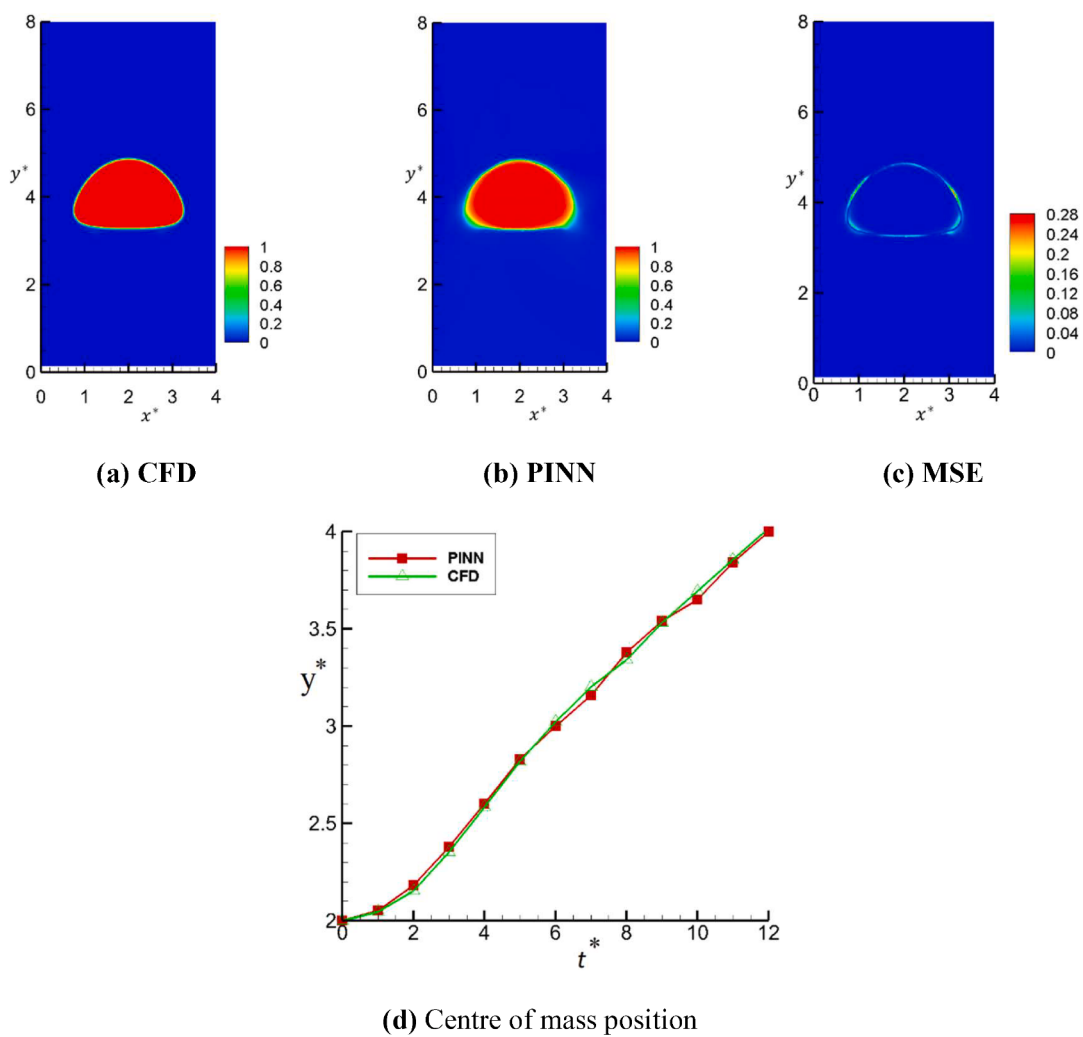


Fig. 12. Predictions for the inverse PINN modelling strategy at $Re = 50$; the system predicted this behaviour only by solving PDEs, since only training data with $Re = 35$ was provided.

well. The other major artefact indicating the effect of the bubble on heat transfer is the compression of the warmest band of fluid at the interfacial front where the bubble completes its approach to the wall.

Applying a Dirichlet boundary condition to enforce the value of T^* at

the hot wall reduced the maximum error (Er_T) by 27% compared to when the condition was detected solely by inference of the PINN. Without specifying this condition, the algorithm struggled to predict the true maximum temperature on the hot wall ($T^* = 1.0$) along its entirety,

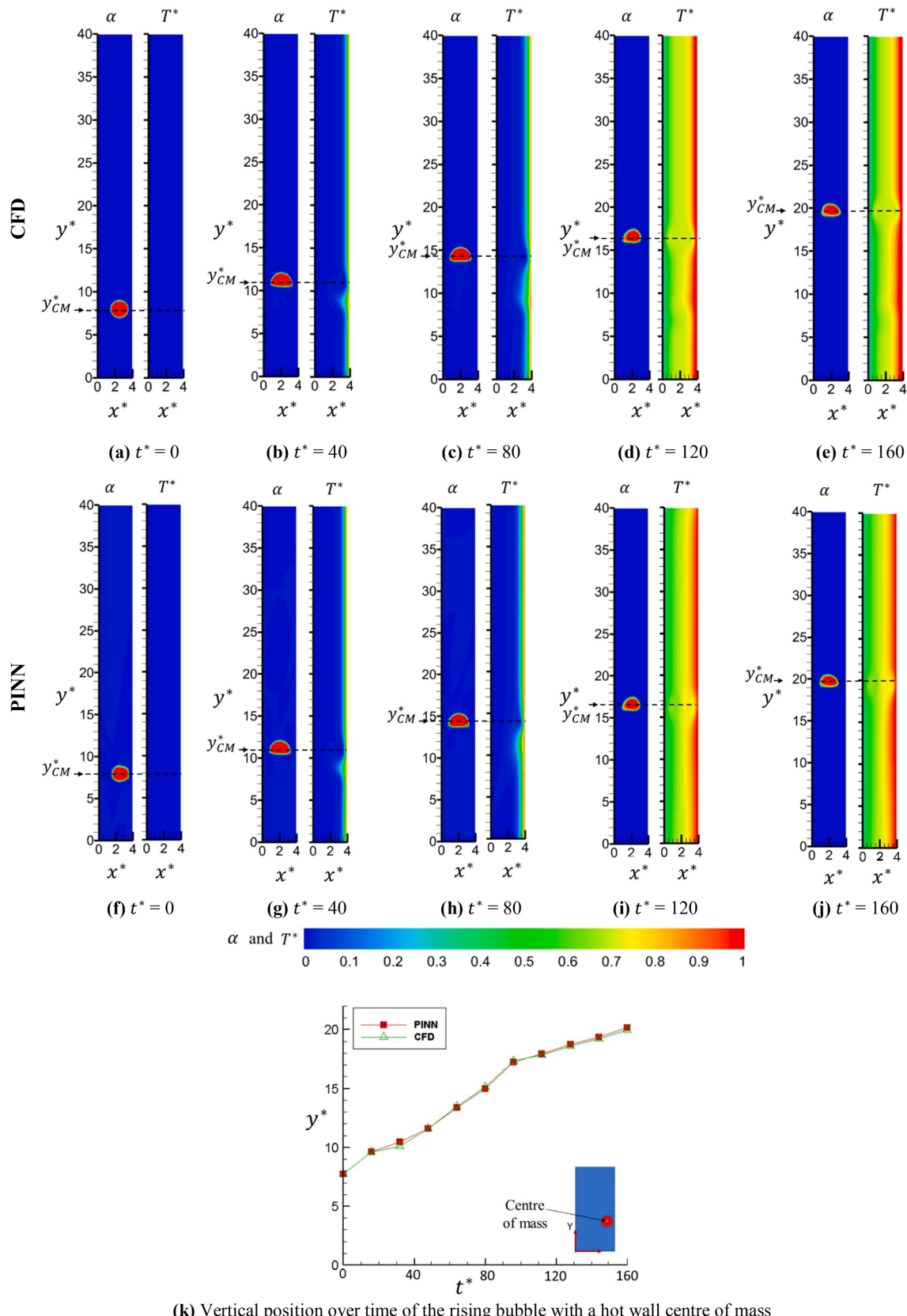


Fig. 13. (a-j) Contours of volume fraction (α) and temperature (T^*) predicted by the CFD (Top) and PINN (Bottom) for the evolution of flow showing how the rising bubble influences the thermal boundary layer on the wall. (k) predictions of bubble centre of mass height over time for CFD and PINN.

though the thermal effect of the wake-vortex interaction was captured well by 1230 CPU hours. In comparison, the effect of directly imposing this boundary condition had a negligible effect on the predicted position of the bubble phase. Without the boundary condition imposed, there was a maximum error (Er_{CM}) at the perimeter of the bubble phase of 16%. Without thermal boundary conditions, an accurate bubble centre of mass position was obtained within 750 CPU hours; the error remained at around 2% for the duration of the analysis.

As with the volume fraction predictions, the inferred temperature field is an accurate representation of the true behaviour. The field inhibits any non-physical diffusion. Quantitative analysis of the temperature contour illustrates that the effect of the bubble wake on the temperature distribution was accurately inferred overall. The only minor discrepancy is that the PINN prediction has underpredicted the size of the thermal boundary layer in the wake of the bubble. However, this is inconsequential as the position and size of the initial wake are captured correctly. The assumptions made by visual inspection are confirmed by quantitative plots of the thermal field at various locations (Fig. 14(a-d)). At the mid-point of the simulation time ($t^* = 80$), the only major quantitative discrepancy is the thickness of the thermal boundary layer above the region affected by the bubble (i.e., $y^* = 20$). For a temperature of $T^* = 0.2$, the x^* position is overpredicted by 7%. However, the general trend is very good and both bounding limits are correctly captured. When combined, the thermal and interfacial solvers work in harmony to accurately determine the effect of the bubble wake on the hot wall.

5. Conclusions

In this study, a physics-informed neural network (PINN) has been developed which solves for both energy and phase interface, addressing several physical phenomena that have been previously underexplored. These include the co-dependant effects of thermal and hydrodynamic boundary layers, flow separation, vortical wakes, buoyancy, and deforming interfaces. Through two-phase case studies, we have evaluated the accuracy of the proposed PINN methodology. These findings demonstrate that the PINN approach is agnostic to geometric and boundary conditions, significantly expanding the capability of PINNs to create reliable and flexible models for two-phase cases, particularly in the study of boiling flows. The algorithm has been demonstrated to be a robust and accurate tool to infer system behaviour for a range of fluid properties and unobserved fields. For hidden field reconstruction, the algorithm reproduced velocity fields aligned with ground-truth CFD data, while the novel application of extrapolative inverse modelling produced a peak MSE of 0.27 and maximum position of mass error of less than 2% over the temporal domain.

The impact of directly imposing boundary conditions on solution accuracy has been quantified, specifically focusing on the rising bubble with hot wall and cylinder geometries. With the incorporation of these boundary conditions, results demonstrate a reduction of maximum thermal error by up to 27.1%, rendering it negligible. Consequently, future research endeavours should carefully consider which behaviours need to be inferred and which can be specified as boundary conditions from the outset. Notably, this algorithm successfully tracked the rising

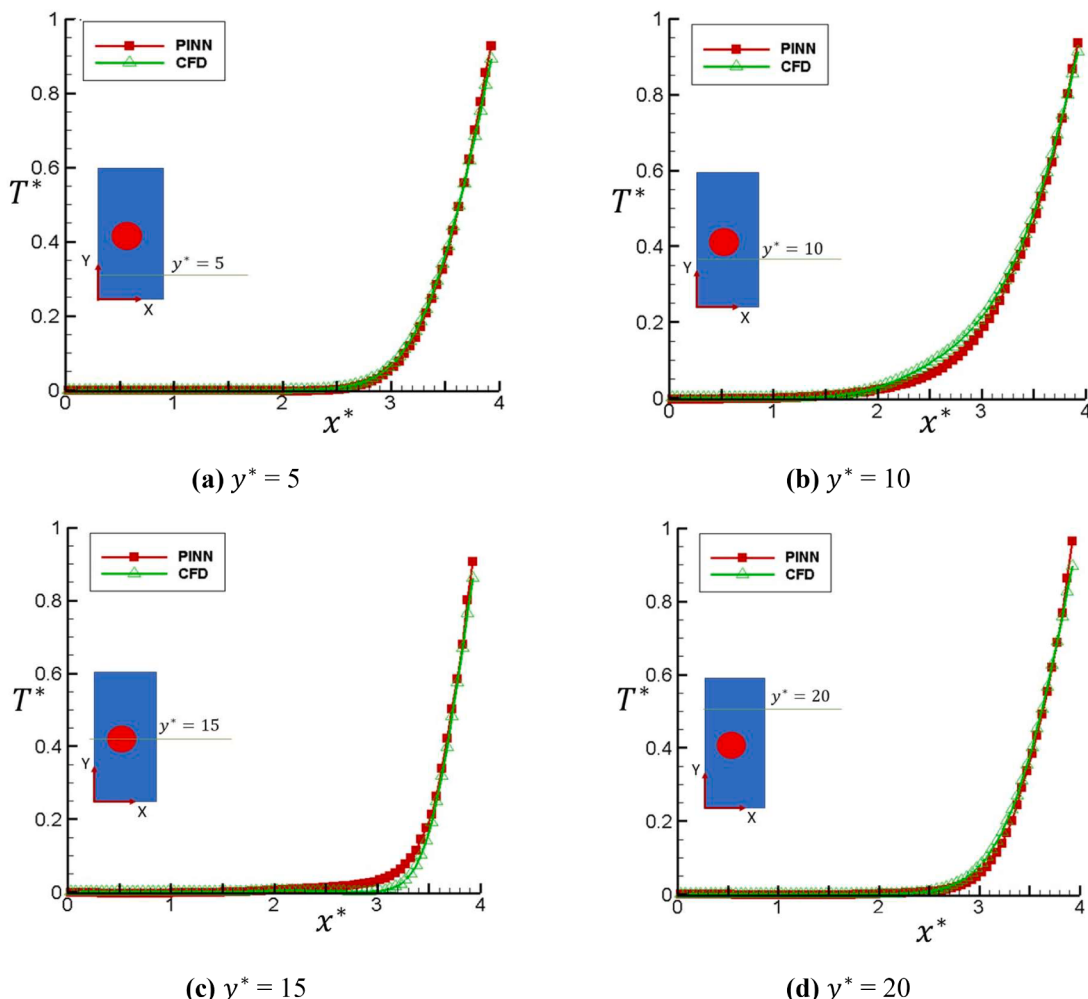


Fig. 14. Analysis of spanwise variation in the temperature field (T^*) due to the wake-wall interaction of the rising bubble at different vertical positions for $t^* = 80$.

bubble with a maximum error of just 2.8% in the centre of mass position and 6.8% at a single extremity of the interface without imposing additional boundary conditions beyond the fluid properties.

The major highlight of this work lies in the ability of the PINN to infer the conjugate effect of buoyancy and natural convection on bubble motion, exemplified by the resulting zig-zag behaviour. Furthermore, the PINN accurately predicted the impact of wake vortices on fluid temperature near the hot wall, with maximum errors of only 3.6% and 6.8% in the multiphase and thermal predictions, respectively, and other error values remained below 1%. Therefore, this work has created a physics-informed flow solver which can accurately resolve complex multiphase fluid flow problems which include heat transfer over a range of geometries encountered in real-world cases.

In future work, the authors intend to incorporate phase saturation into the proposed methodology, enabling a better understanding of temperature-dependant phase change using the PINN approach. Additionally, further study will address the somewhat granular nature of PINN-inferred interfaces to achieve flow reconstruction that matches the accuracy provided by traditional methods such as computational fluid dynamics. With the capabilities demonstrated in this paper, the authors will explore the study of nucleate boiling using PINN methods.

CRediT authorship contribution statement

Darioush Jalili: Conceptualization, Data curation, Formal analysis, Investigation, Methodology, Resources, Software, Validation, Visualization, Writing – original draft, Writing – review & editing. **Seohee Jang:** Investigation, Resources. **Mohammad Jadidi:** Data curation, Formal analysis, Investigation, Methodology, Project administration,

Appendix

A.1. Overview of single-phase test cases

To best optimise the prediction abilities of PINN, key physics needed to be isolated and tested in sequence. Studying the physics of vortical wake structures, thermal and momentum boundary layers, could be carried out effectively in single-phase cases. Ultimately, this isolation approach meant the preparatory work for a conjugate solver could be accelerated.

A.1.1. Flow over a hot cylinder test case

Natural convective heat transfer between a cylinder and its surroundings is a common generalisation for systems such as heat exchangers, nuclear fuel rods, energy storage devices and solar collectors [48]. It was important to validate wake predictions on this model, which is well-documented in the literature because the eventual aim of this work was to determine how wake behaviour affects heat transfer in two-phase flows. This work simulates a Von Karman vortex street [49]. Under this regime, alternating vortices travel along the streamwise direction. In this case, both the incompressible Navier-Stokes and transient energy equations must be satisfied. Unlike cases seen in literature, each variable of interest is provided with its own neural network to assess system accuracy in cases where a divergence-free approximation cannot be used. In this case, the global Reynolds number is 200. A flow-through time of 8 s was used here. Additionally, the cylinder wall maintained a constant hot temperature ($T_{bulk} = 1$), while fluid at the inlet maintained a cold temperature ($T_{bulk} = 0$) (Fig. 2(a)). Thermal and velocity-based boundary conditions were imposed on the cylinder region in the PINN methodology to reduce computational demand.

The full domain of 8581 collation points at cell centres was provided as training data, meaning the ML algorithm observed flow behaviour which encompasses a Karman Vortex Street, a stagnation point at the front of the cylinder and non-slip boundaries at the top and bottom of the domain. According to Raissi et al. [20], development of the vortex must be captured at a minimum of 5 increments to ensure the algorithm can infer to a sufficient degree of accuracy. To improve the accuracy of predictions, this simulation made use of adaptive weights. Using the neural tangent kernel (NTK) methodology [50], the nodal outputs (weights and biases) were adjusted every 100 epochs. An NTK with sufficient width can consistently drive neural networks to converge upon the global minimum, meaning the network is less sensitive to assumptions made at initialisation. Quantitative results are shown in Fig. A.1, which show strong agreement to ground truth (CFD) data.

Resources, Software, Supervision, Validation, Visualization, Writing – original draft, Writing – review & editing. **Giovanni Giustini:** Supervision, Writing – review & editing. **Amir Keshmiri:** Project administration, Supervision, Writing – review & editing. **Yasser Mahmoudi:** Conceptualization, Funding acquisition, Investigation, Project administration, Resources, Supervision, Writing – review & editing.

Declaration of Competing Interest

The authors declare that they have no known competing financial interests or personal relationships that could have appeared to influence the work reported in this paper.

Data availability

Data will be made available on request.

Acknowledgements

This work was partially supported by the UK Engineering and Physical Sciences Research Council (EPSRC) [grant numbers EP/W033542/1, EP/T012242/2 and EP/T027061/2]. Data supporting this publication can be obtained on request. The authors would like to acknowledge the assistance given by Research IT and the use of the Computational Shared Facility at The University of Manchester. The authors would also like to express their appreciation for the valuable contributions made to the literature survey by Melvin Sebastian MSc.

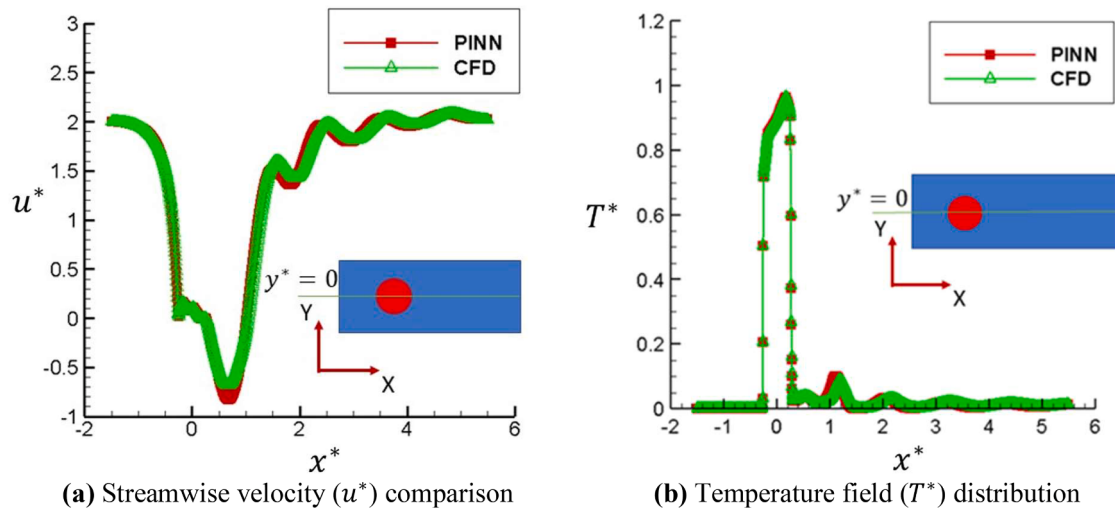


Fig. A.1. Quantitative comparison of (a) streamwise velocity and (b) temperature distribution for the flow around a heated cylinder case at $y^* = 0$ when $t^* = 15$.

A.1.2. Single-phase channel flow with heat transfer test case

Despite their relative simplicity, research on two-dimensional flows in smooth channels is still garnering significant attention. This is thanks to the sustained interest in shrinking electronic circuit boards, the prominence of battery power and subsequent thermal controls for these systems. Under these conditions, the developing boundary layer decreases the local Nusselt number. Therefore, an accurate representation of the momentum boundary layer is contingent on producing a realistic temperature field. The channel geometry was of particular interest in ascertaining the accuracy of the PINN solver used in this work as it allows the physics behind inferring thermal and velocity boundary layers to be isolated. This was important in preparing the algorithm for the rising bubble with energy case. The case study chosen for this work was based on the work by Laubscher [20]. The geometry of the channel is depicted in Fig. 2(b), alongside important thermofluidic properties. In this case, the north and south walls of the channel are maintained at a constant cold temperature ($T_{bulk} = 0$) while hot fluid ($T_{bulk} = 1$) enters the domain with $Re = 100$. No flow crosses the north or south walls. Both the momentum and heat transfer behaviours consisted solely of a developing boundary layer; so just 4400 CFD cells were provided as training data. The flow through time in this case was 10 s.

A.2. Summary of training data used

A summary of training data for each test case is provided in this section. Each mesh used a uniform distribution of quadrilateral cells. Table A.1 details all relevant parameters including collocation points, mesh cell resolution and total number of timesteps provided in each case. Collocation points are defined as points at which the network calculates error in PDE solution predictions, while mesh cell sites provide data for the algorithm to calculate residual loss. The inferred ellipsoidal rising bubble case received an incomplete dataset, while the inferred spherical cap case received no CFD data at all.

Table A.1

CFD data provided for training of each case study.

| Case | Collocation points | Mesh resolution | Timesteps of data provided (of total) |
|--|--------------------|-----------------|---------------------------------------|
| Immiscible channel flow | 4400 | 4400 | 15 (20) |
| Ellipsoidal rising bubble | 25,000 | 25,000 | 45 (60) |
| Skirted rising bubble | 25,000 | 25,000 | 45 (60) |
| Rising bubble with a hot wall | 26,321 | 26,321 | 500 (1000) |
| Inferred ellipsoidal rising bubble | 25,000 | 25,000 | 45 (60) |
| Inferred spherical cap | 25,000 | 0 | 0 |
| Single-phase flow over a hot cylinder | 8581 | 8581 | 150 (200) |
| Single-phase channel flow with heat transfer | 4400 | 4400 | 15 (20) |

References

- [1] A. Korolev, P.R. Field, The effect of dynamics on mixed-phase clouds: theoretical considerations, *J. Atmos. Sci.* 65 (1) (2008) 66–86.
- [2] C.R. Kharangate, I. Mudawar, Review of computational studies on boiling and condensation, *Int. J. Heat Mass Transf.* 108 (2017) 1164–1196. A.
- [3] T.J. Lin, K. Tsuchiya, L.S. Fan, Bubble flow characteristics in bubble columns at elevated pressure and temperature, *AIChE* 44 (3) (2004) 545–560.
- [4] J. Lee, H. Park, Wake structures behind an oscillating bubble rising close to a vertical wall, *Int. J. Multiphase Flow* 91 (1) (2017) 225–242.
- [5] J. Hua, J. Lou, Numerical simulation of bubble rising in viscous liquid, *J. Comput. Phys.* 222 (2007) 769–795.
- [6] K. Choi, H. Park, Interfacial phenomena of the interaction between a liquid–liquid interface and rising bubble, *Exp. Fluids* 62 (1) (2021) 126.
- [7] Y. Fan, J. Fang, I. Bolotnov, Complex bubble deformation and break-up dynamics studies using interface capturing approach, *Exp. Comput. Multiph. Flow* 3 (1) (2020) 139–151.
- [8] S. Cuomo, V.S.D. Cola, F. Giampaolo, G. Rozza, M. Raissi, F. Piccialli, Scientific machine learning through physics-informed neural networks: where we are and what's next, *J. Sci. Comput.* 92 (1) (2022) 88.
- [9] F.F.d.l. Mata, A. Gijón, M. Molina-Solana, J. Gómez-Romero, Physics-informed neural networks for data-driven simulation: advantages, limitations, and opportunities, *Phys. A* 610 (2023), 128415.

- [10] S. Cai, Z. Mao, Z. Wang, M. Yin, G.E. Karniadakis, Physics-informed neural networks (PINNs) for fluid mechanics: a review, *Acta Mech. Sin.* 37 (2021) 1727–1738.
- [11] E. Zhang, M. Dao, G.E. Karniadakis, S. Suresh, Analyses of internal structures and defects in materials using physics-informed neural networks, *Sci. Adv.* 8 (7) (2022).
- [12] M. Raissi, P. Perdikaris, G.E. Karniadakis, Machine learning of linear differential equations using Gaussian processes, *J. Comput. Phys.* 348 (1) (2017) 683–693.
- [13] M. Raissi, A. Yazdani, G.E. Karniadakis, Hidden Fluid Mechanics: a Navier-Stokes Informed, *Science* 367 (6481) (2020) 1026–1030.
- [14] J.H.F. Piouch, A. Müller, F.J. Peitzmann, D. Schramm, O. el Moctar, Turbulence modeling for physics-informed neural networks, *Fluids* 8 (43) (2023) 1–17.
- [15] X. Jin, S. Cai, H. Li, G.E. Karniadakis, NSFnets (Navier-Stokes flow nets):physics-informed neural networks for the incompressible Navier-Stokes equations, *J. Comput. Phys.* 426 (1) (2021), 109951.
- [16] S. Cai, Z. Wang, F. Fuest, Y. Jeon, C. Gray, G. Karniadakis, Flow over an espresso cup: inferring 3-D velocity and pressure fields from tomographic background oriented Schlieren via physics-informed neural networks, *J. Fluid Mech.* 915 (102) (2021) 1–17.
- [17] Q. Zhu, Z. Liu, J. Yan, Machine learning for metal additive manufacturing: predicting temperature and melt pool fluid dynamics using physics-informed neural networks, *Comput. Mech.* 67 (1) (2021) 619–635.
- [18] S. Niaki, E. Haghigheh, T. Campbell, A. Pourartip, R. Varzi, Physics-informed neural network for modelling the thermochemical curing process of composite-tool systems during manufacture, *Comput. Methods Appl. Mech. Eng.* 384 (1) (2021).
- [19] S.B.L. Papadopoulos, S. Nikolopoulos, I. Kalogeris, V. Papadopoulos, A computational framework for the indirect estimation of interface thermal resistance of composite materials using XPINNs, *Int. J. Heat Mass Transf* 200 (1) (2023) 1–14.
- [20] R. Laubscher, Simulation of multi-species flow and heat, *Phys. Fluids* 33 (1) (2021) 1–14.
- [21] Alex Royer, O. Farges, P. Boulet, D. Burat, A new method for modeling radiative heat transfer based on Bayesian artificial neural networks and Monte Carlo method in participating media, *Int. J. Heat Mass Transf* (1) (2023) [Online] Available, <http://www.sciencedirect.com.manchester.idm.oclc.org/science/article/pii/S0017931022010791>.
- [22] X. Zhao, R.K. Salko, K. Shirvan, Improved departure from nucleate boiling prediction in rod bundles using a physics-informed machine learning-aided framework, *Nucl. Eng. Des.* 374 (1) (2021).
- [23] A.B. Buhendwa, S. Adami, N.A. Adams, Inferring incompressible two-phase flow fields from the interface motion using physics-informed neural networks, *Mach. Learn Appl.* 4 (1) (2021).
- [24] R. Qiu, et al., Physics-informed neural networks for phase-field method in two-phase flow, *Phys. Fluids* 34 (5) (2022), 052109.
- [25] H. Zhai, Q. Zhou, G. Hu, Predicting micro-bubble dynamics with semi-physics-informed deep learning, *AIP Adv* 12 (3) (2022), 035153.
- [26] C.W. Hirt, B.D. Nichols, Volume of fluid (VOF) method for the dynamics of free boundaries, *J. Comput. Phys.* 39 (1) (1981) 201–225.
- [27] Ameya D. Jagtap, Kenji Kawaguchi, and G.E. Karniadakis, "Locally adaptive activation functions with slope recovery for deep and physics-informed neural networks," in *Proc. R. Soc. A*, 2020, vol. 476, no. 1, p. 20200334.
- [28] N.S. Keskar and R. Socher, "Improving generalization performance by switching from adam to SGD," arXiv preprint, Ithaca, NY, 2017.
- [29] D.P. Kingma, L.J. Ba, Adam: a Method for Stochastic Optimization. Amsterdam Machine Learning Lab (IVI, FNWI), Amsterdam, NL, 2015.
- [30] S. Hysing, et al., Quantitative benchmark computations of two-dimensional bubble dynamics, *Int. J. Numer. Methods Fluids* 60 (11) (2009) 1173–1290.
- [31] M. Rezavand, M. Taeibi-ahni, W. Rauch, AN ISPH scheme for numerical simulation of multiphase flows with complex interfaces and high density ratios, *Comput. Math. Appl.* 75 (1) (2018) 2658–2677.
- [32] D. Bhaga, M.E. Weber, Bubbles in viscous liquids: shapes, wakes and velocities, *J. Fluid Mech.* 105 (1) (1981) 61–85.
- [33] M. Aliakbari, M. Mahmoudi, P. Vadasz, A. Arzani, Predicting high-fidelity multiphysics data from low-fidelity fluid flow and transport solvers using physics-informed neural networks, *Int. J. Heat Fluid Flow* 96 (1) (2022).
- [34] D. Lucor, A. Agrawal, A. Sergeant, Simple computational strategies for more effective physics-informed neural networks modeling of turbulent natural convection, *J. Comput. Phys.* 456 (1) (2022).
- [35] R. Lonher, H. Antil, H. Tamaddon-Jahromi, N. Chaksu, P. Nithiarasu, Deep learning or interpolation for inverse modelling of heat and fluid flow problems? *Int. J. Numer. Methods Heat Fluid Flow* 31 (9) (2021).
- [36] D. Joseph, Rise velocity of a spherical cap bubble, *J. Fluid Mech.* 488 (1) (2003) 213–223.
- [37] M. Tripathi, K. Sahu, R. Govindarajan, Dynamics of an initially spherical bubble rising in quiescent liquid, *Nat. Commun* 6 (6268) (2015).
- [38] M. Mccartney, M. Haeringer, W. Polifke, Comparison of machine learning algorithms in the interpolation and extrapolation of flame describing functions., presented at the ASME, *J. Eng. Gas Turbines Power* (2020).
- [39] L. Sun, H. Gao, S. Pan, J.X. Wang, Surrogate modeling for fluid flows based on physics-constrained deep learning without simulation data, *Comput. Methods Appl. Mech. Eng.* 361 (1) (2020).
- [40] W. Liu, J. Fang, S. Rolfo, C. Moulinec, D. Emerson, On the improvement of the extrapolation capability of an iterative machine-learning based RANS Framework, *Comput. Fluids* 256 (1) (2023).
- [41] J.C. Cano-Lozano, R. Bolanos-Jiménez, C. Gutiérrez-Montes, C. Martínez-Bazán, The use of Volume of Fluid technique to analyze multiphase flows: specific case of bubble rising in still liquids, *Appl Math Model* 39 (12) (2015) 3290–3305.
- [42] J. Kim, Review of nucleate pool boiling bubble heat transfer mechanisms, *Int. J. Multiphase Flow* 35 (2009) 1067–1076.
- [43] P. Bhuvankar, S. Dabiri, Impact of a single bubble rising near a wall on the wall-to-liquid heat flux, *Int. J. Heat Mass Transf* 116 (2018) 4445–4457.
- [44] H. Maeng, H. Park, An experimental study on the heat transfer by a single bubble wake, *Int. J. Heat Mass Transf* 165 (1) (2021) 1–17.
- [45] M.M. Larimi, A. Ramiar, Two-dimensional bubble rising through quiescent and non-quiescent fluid, *Int. J. Therm. Sci.* 131 (1) (2018) 58–71.
- [46] N.G. Deen, J.A.M. Kuipers, Direct numerical simulation of wall-to-liquid heat transfer in dispersed gas-liquid two-phase flow using a volume of fluid approach, *Chem. Eng. Sci.* 102 (1) (2013) 268–282.
- [47] S. Wang, X. Yu, P. Perdikaris, When and why PINNs fail to train: a neural tangent kernel perspective, *J. Comput. Phys.* 449 (2022) 1–28.
- [48] D.G. Roychowdhury, S.K. Das, T. Sundarajan, Numerical simulation of natural convective heat transfer and fluid flow around a heated cylinder inside an enclosure, *Heat Mass Transfer* 38 (1) (2002) 565–576.
- [49] T. Von Karman, Aerodynamics - History and Analysis of Flight, McGraw-Hill, Ithaca, NY, 1963.
- [50] A. Jacot, F. Gabriel, C. Hongler, Neural tangent Kernel: convergence and generalization in neural networks, in: Proceedings of the Conference on Neural Information Processing Systems NeurIPS, Montreal, CA, 2018.